POLITECNICO DI MILANO

School of Industrial and Information Engineering

Department of Physics

MSc in Engineering Physics

NARROWBAND PHONON PUMPING FOR THE INVESTIGATION OF LIGHT-INDUCED SUPERCONDUCTIVITY

Supervisor:
Prof. Giulio CERULLO
Prof. Andrea CAVALLERI

Co-supervisor:
Prof.ssa Arianna MONTORSI

Author:
Antonio PICANO
ID Number: 859464

Academic Year 2016–2017

Abstract

The large-amplitude coherent mid-infrared excitation of apical oxygen oscillations in bilayer cuprates $YBa_2Cu_3O_{6+x}$ is known to promote a short-lived superconducting-like state even far above the critical temperature. Subsequent time-resolved x-ray diffraction experiments showed that the nonlinear coupling of the resonantly driven apical oxygen phonon mode to a set of Raman-active modes induces a transient crystal structure likely to favour this out-of-equilibrium superconductivity.

However, the splitting of the apical oxygen vibrations into lower- and higher- frequency modes at 16.5 and 19.3 THz – corresponding to the oscillations of the apical oxygen atoms in the oxygen-rich and oxygen-deficient Cu-O chains, respectively – was disregarded in these studies. The two modes were indeed excited simultaneously because the broadband driving pulses available (30 % $\frac{\Delta E}{E}$ bandwidth) didn't allow to distinguish between them.

Here, we present a mid-infrared pulsed light source sufficiently narrowband and tunable to drive separately the two near-degenerate apical oxygen phonon modes in the bilayer cuprate $YBa_2Cu_3O_{6.5}$. By exploiting chirped pulse difference frequency generation in GaSe nonlinear crystal, we managed to produce carrier-envelope phase stable pulses, tunable between 16 THz and 23 THz, with a minimum relative bandwidth $\frac{\Delta E}{E}$ of 2%. The bandwidth of these pulses scaled linearly with their time duration, which can be chosen, by the amount of chirp imprinted on the generating near-infrared pulses, between 200 fs and 1 ps. The energy of the mid-infrared pulses, around 8 μJ, could be kept constant even for different pulse durations by adjusting the spot sizes of the generating NIR pulses in the GaSe nonlinear crystal to maintain the gain coefficient.

By means of this source, we were able to clearly distinguish, possibly for the first time, the effect of each of the two vibrational modes on the light-induced superconducting state. The data from pump-probe time-resolved THz-spectroscopy showed that the strength of the transient superconducting coupling between bilayers above the equilibrium critical temperature – measured through the value of transient superfluid density along the c-axis, ρ_c – scales linearly with the amplitude of the driving electric field. According to the theory of nonlinear phononics, this implies that ρ_c scales with the square root of the normal coordinate Q_R of the Raman mode associated with the reduction in the distance between bilayers. Futhermore, ρ_c was found to assume a much higher value for the phonon at 19.28 THz that, between the two investigated, has the biggest spectral weight.

These conclusions may help finding optimized routes for enhancing superconductivity with light and for making this transient states long-lived, in view of possible applications.

Contents

List of Figures

Chapter 1

Introduction

Over the last three decades, we have seen a spectacular technological progress in ultrashort pulse generation. This has been possible thanks to the realization of solid-state laser systems, mainly based on Ti:sapphire [27] or Yb:doped gain media. These systems generate pulses of near-infrared femtosecond time duration and, in addition, show high peak powers. For these reasons they offer the unique opportunity of strongly driving materials out of their equilibrium, and simultaneously monitoring their temporal evolution at the fundamental time scales of atomic and electronic motion.

One can imagine both fundamental and real-world applications, for example ultrafast non-volatile data storage photonic devices. In materials with strong electronic correlations, a plethora of phenomena have already been observed when they are optically perturbed - like photo-induced insulator-to-metal transition achieved by *photo-doping* Mott insulators [28] [29], optical melting of magnetic order [30] [31], or excitation of coherent orbital waves– and the capability of controlling them opens the possibility of exploit them at will. However, stimulation with near-infared or visible ($\approx$eV) photons can lead to strong limitations in terms of control capability, as they directly

couple to electronic excitations and inevitably heat up the electronic system. Thus, switching between phases by reversing transitions with subsequent light pulses, as necessary for storage devices, is not possible.

One approach to overcome this problem is to directly drive materials resonantly with the energies of the above mentioned low excitations, that lie below 100 meV. With the power transferred directly into structural motions, dissipation of heat into the electronic system is strongly reduced. This allowed to control insulator-metal transitions, melting of magnetic order and light-induced superconductivity [47] [33] [34], by means of coherent excitation of infrared-active lattice vibrations by THz light pulses. The origin of this powerful tool lies in the nonlinear nature of the crystal lattice. Infrared-active phonons driven by THz pulses to large amplitudes can couple anharmonically to lower-frequency Raman-active vibrational modes, to exert transient and directional distortion of the crystal structure.

Here we focus on transiently enhanced interlayer superconducting coupling far above T_c in underdoped $YBa_2Cu_3O_{6+x}$, induced by resonant femtosecond mid-infrared light pulses. These materials are made by bilayers of CuO_2 planes, separated by an insulating layer, as sketched in Figure 1.1. The interbilayer region contains, as well as Yttrium atoms, $Cu-O$ chains along the out-of-plane c-axis and along the crystal b axis. In the particular case of $YBa_2Cu_3O_{6.5}$, these last are alternatively oxygen-rich and oxygen-deficient. At equilibrium, the low-temperature superconducting phase involves coherent tunnelling between stack of bilayers, that is lost above the transition temperature. By resonantly driving oscillations of the apical oxygen atoms in the Cu-O chains, the coherent inter-bilayer tunnelling was shown to be transiently restored above the critical temperature for a few picoseconds. Time-resolved x-ray diffraction experiments showed that the nonlinear cou-

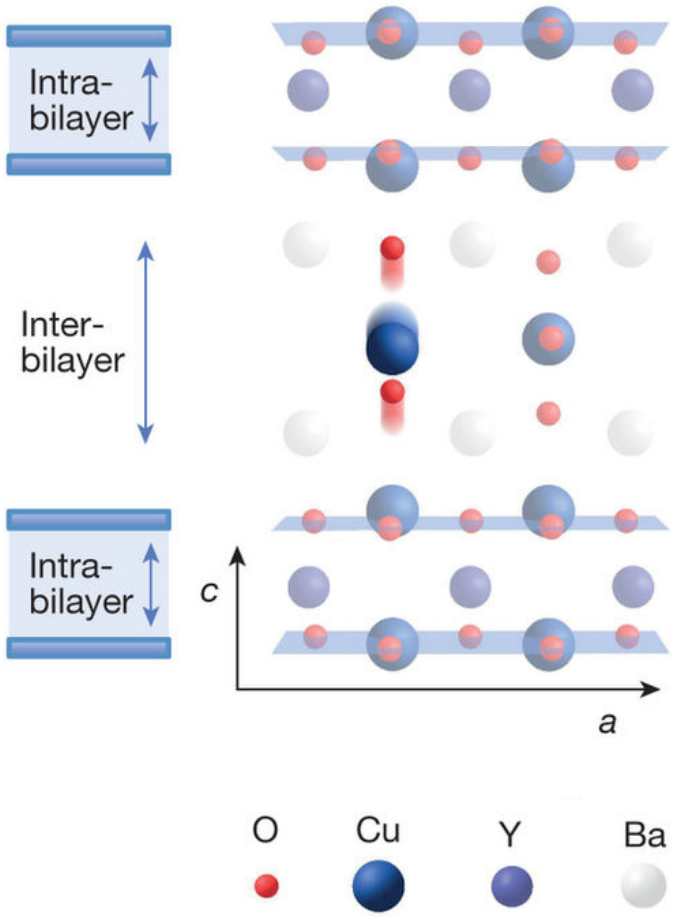

Figure 1.1: Structure of $YBa_2Cu_3O_{6.5}$ and motion of the apical oxygen at the empty chain sites. On the left, schematic representation of the inter- and intra- bilayer regions.

pling of this apical oxygen mode to a certain set of Raman-active modes causes a reduction of the distance between bilayers [37]. This distance reduction can intuitively justify the restoring of interbilayer coupling in the transient state above T_c.

Actually, in $YBa_2Cu_3O_{6.5}$, there are two phonon modes associated with the oscillation of apical oxygen atoms: one, at a frequency of 16.5 THz, drives the atoms in the oxygen-rich Cu-O chain, while the other at 19.3 THz drives oscillations in the oxygen-deficient Cu-O chains. Obviously, the two modes are very close in frequency so, to date, they could have been driven only simultaneously by broadband ($\approx 30\%\frac{\Delta E}{E}$ bandwidth) pump pulses. The goal of the thesis is to setup - by exploiting the chirped pulse difference frequency generation mechanism - a source that is sufficiently narrowband to drive the two apical oxygen modes separately and pave the way for a better understanding of the light-induce superconductivity in underdoped cuprates.

The thesis is structured as follows. In Chapter 2, the methods for the generation and detection of THz and MIR pulses are described. Particular focus is posed on how to select the proper nonlinear crystal. In Chapter 3, the experimental setup for the generation of narrowband MIR pulses by means of difference frequency generation between two linearly chirped NIR pulses is shown. In Chapter 4, the light-induced state of YBCO is discussed, together with the evidences that the theory of nonlinear phononics can represent a valid tool for the justification of this phenomenon. In Chapter 5, the methods of the time-resolved pump-probe spectroscopy are summarized and the results from our experimental setup are discussed. Follow Conclusions and Outlook.

Chapter 2

Generation and Detection of intense THz and MIR pulses

The *terahertz* (1 THz = 10^{12} Hz) frequency range is usually defined as the part of the electromagnetic spectrum spanning from around 0.1 THz to 10 THz; the *mid-infrared* (MIR), from 10 to 50 THz. The most effective generation methods that produce carrier-to-envelope phase (CEP) stable pulses and high peak field strengths in the region across THz and MIR are based on *difference frequency generation* (DFG) - and on *optical rectification* (OR) - in nonlinear materials. We first describe the physics of DFG and the criteria for efficient THz and MIR generation. Then, we analyse the characteristics of the materials that fulfil these criteria. Finally, we demonstrate that pulses generated with these techniques are CEP stable.

2.1 DFG and OR: basic principles

A linearly polarised laser pulse $E(z,t)$, during propagation in a medium in direction z, induces a polarisation:

$$P(z,t) = P_L(z,t) + P_{NL}(z,t). \tag{2.1}$$

Here, $P_L(z,t)$ is the *linear polarisation* - coupled to $E(z,t)$ by the *linear susceptibility tensor* $\chi^{(1)}$ - , and $P_{NL}(z,t)$ is the *nonlinear* term induced by strong electric field and depending on $E^2, E^3, \ldots$ [1][2]. Without taking into account, for the moment, spatial and temporal dispersion in the nonlinear medium, the nonlinear polarisation $P_{NL}(z,t)$ can be written as:

$$P_{NL}(z,t) = \epsilon_0 \chi^{(2)} E^2(z,t) = 2\epsilon_0 d_{eff} E^2(z,t) \tag{2.2}$$

where d_{eff} is the so-called *effective nonlinear optical coefficient*, which depends on the specific components of the *second-order nonlinear tensor* $\chi^{(2)}$ involved in the interaction. We are limiting our analysis to second-order effects, by neglecting the dependence of the nonlinear polarisation $P_{NL}(z,t)$ on $\chi^{(3)}$ and higher orders, since they do not contribute to the THz generation.

According to Maxwell's equations, written in the scalar approximation and in SI units, the evolution of the field $E(z,t)$ can be described by:

$$\frac{\partial^2 E(z,t)}{\partial z^2} - \mu_0 \frac{\partial^2 D(z,t)}{\partial t^2} = \mu_0 \frac{\partial^2 P_{NL}(z,t)}{\partial t^2} \tag{2.3}$$

where $D(z,t) = \epsilon_0 E(z,t) + P_L(z,t)$ is the *electric displacement field*. As we can see, $\frac{\partial^2 P_{NL}(z,t)}{\partial t^2}$ act as a source term for radation at frequencies different from the ones present in the initial driving field.

If we consider an ideal optical field consisting of only two frequency com-

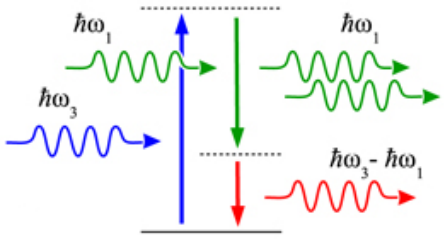

Figure 2.1: From [1]. Simple model of difference frequency generation: the photon at higher energy, $\hbar\omega_3$ is absorbed by a virtual level of the nonlinear material in which it interacts with another photon at frequency ω_1; the photon at ω_1 stimulates the emission of a photon at ω_1. For energy conservation reasons, also a photon at ω_2 is generated: $\hbar\omega_2 = \hbar\omega_3 - \hbar\omega_1$.

ponents, ω_3 and ω_1, that impinges upon a second-order noncentrosymmetric nonlinear optical medium, the source term in 2.3, expressed according to 2.2, will contain components at frequencies $2\omega_3$ and $2\omega_1$ (*second harmonic generation*, SHG), $\omega_1 + \omega_3$ (*sum frequency generation*, SFG) and $\omega_3 - \omega_1$ (*difference frequency generation*, DFG). We are interested in the DFG process: through the nonlinear interactions between the spectral components, the field at higher frequency, ω_3, loses energy in favour of the one at ω_1 and a new field at frequency $\omega_2 = \omega_3 - \omega_1$ is generated (in Figure 2.1 also the corpuscular interpretation). When $\omega_3 \approx \omega_1$, the limit process is called *optical rectification* (OR).

Notice that the electromagnetic field we have taken into account can represent either two wavepackets whose center frequencies are ω_3 and ω_1, or a single laser pulse, in which ω_3 and ω_1 are two frequency components that we chose arbitrarily within its spectrum. In practice in DFG, that is usually used to generate radiation in the MIR, we are referring to the first situation, whilst in OR, that is used to generate THz radiation, to the second one. OR is the result of DFG between the spectral components of a single laser pulse.

2.2 Generation of THz pulses via OR

In this section we will show the conditions for optimized THz generation through OR. We consider subpicosecond optical pump pulses passing through a nonlinear optical material. We relax the hypothesis of nondispersive medium. In this case, equation 2.2 has to be substitute with:

$$P_{NL}(z,t) = \epsilon_0 \iint \chi^{(2)}(t_1,t_2) E(t-t_1) E(t-t_2)\, dt_1 dt_2. \tag{2.4}$$

The induced nonlinear polarization acts as a source of THz radiation in equation 2.3. The absolute value of the emitted THz field $E_{em}(\omega, z)$, for a given pump angular frequency ω_0, that we assume within the material's transparency frequency range, can be written as [3]:

$$|E_{em}(\omega,z)| = \frac{\mu_0 \chi^{(2)}(\omega)\omega I_0(\omega)}{n(\omega_0)[n(\omega)+n_g]} L_{eff}(\omega,z) \tag{2.5}$$

Here: ω stands for THz angular frequencies; $I_0(\omega)$ is the Fourier transformed intensity of the input laser pulse at $z = 0$ inside the crystal ; and $n(\omega_0)$ and n_g are, respectively, the refractive index and the optical group index, both at the carrier frequency of the pump, ω_0.

Equation 2.5 shows that a high second-order nonlinear susceptibility $\chi^{(2)}(\omega)$ is crucial for effective THz generation. At the same time, the amplitude of the emitted radiation is proportional to $L_{eff}(\omega, z)$, a quantity having the unit of a length:

$$L_{eff}(\omega,z) = \sqrt{\frac{1+\exp(-\alpha(\omega)z) - 2\exp\left(-\frac{\alpha(\omega)}{2}z\right)\cos\left(\frac{\omega}{c}[n(\omega)-n_g]z\right)}{[\frac{\alpha(\omega)}{2}]^2 + (\frac{\omega}{c})^2[n(\omega)-n_g]^2}} \tag{2.6}$$

This can be seen, indeed, as an effective length, whose maximum value - rep-

resented by the crystal coordinate z - is reduced by the material dispersion, that causes velocity mismatch ($n(\omega) \neq n_g$), and by nonzero absorption $\alpha(\omega)$ at THz frequencies.

The *velocity matching* or *phase matching* condition ($n(\omega) \approx n_g$) is nothing but the fact that an efficient conversion of the optical intensity $I_0(\omega)$ into THz radiation $E_{em}(\omega)$ requires the phase velocity of the generated THz radiation to match the group velocity of the pump laser pulse.

For what concerns the material absorption, two frequency regions must be taken into account: the one at THz, and the one at $2\omega_0$, $3\omega_0 \ldots$ (remember that we are assuming that the material is transparent at ω_0). In fact, in addition to lattice resonances leading to absorption $\alpha(\omega)$ in spectral regions of the generated THz radiation, two- three- (or even more) photon absorption at frequencies multiple of the carrier frequency ω_0 may happen. This process leads not only to a decrement of the effective pump intensity $I_0(\omega)$, but also to a generation of free carriers inside the medium. The enhancement of free carrier concentration leads to increased absorption of the generated THz radiation, that means it causes saturation of the generated THz energy. To prevent two-phonon absorption from occurring, the wavelength of the incident beam must be at least twice the wavelength that corresponds to the electronic absorption edge of the nonlinear crystal. The lowest order of multi-photn absorption is determined by the ratio of the material bandgap (in case they have a gap, otherwise the frequency of the absorption edge is taken as a reference) to the pump photon energy.

2.2.1 ZnTe and LNO

We have learned in the previous section that the efficiency of THz generation through OR is mainly determined by: the absolute value of the effective

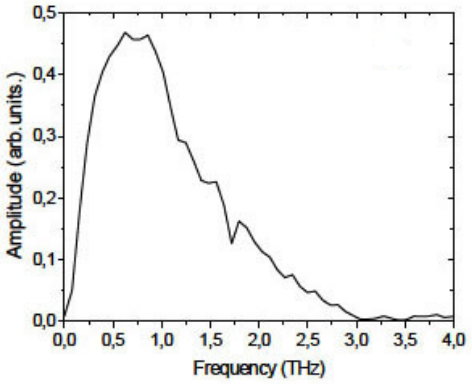

Figure 2.2: From [10]. Spectrum of the THz from ZnTe.

nonlinear coefficient d_{eff}; the value of the refractive index at ω and at ω_0; the length over which velocity matching between THz and optical propagation can be maintained ($L_{eff}(\omega)$); and the absorption in the material. In the following, we will analyse the characteristics of the crystals that have represented the best possible compromise among all these requirements.

ZnTe is appreciated mostly because, pumped at appropriate wavelengths, can *approximately* satisfy the *phase matching* condition in a *collinear* geometry. The optical group index n_g indeed at 800 nm is equal to 3.13; a value that is close to the one of the THz refractive index ($n_{THz} = 3.17$) [21].However, for pump pulses with high peak intensity, this material shows saturation effects due to two-photon absorption. This process, that leads to depletion of the pump beam as well as free-carrier absorption of the THz beam, limits the *energy conversion efficiency* ($\eta_E = E_{pump}/E_{THz}$). In [10], an energy conversion efficiency - from OR in a large-aperture ZnTe single crystal wafer, pumped at 800 nm - of 3.1 x 10^{-5} has been calculated. The generated THz frequency spectrum, shown in Figure 2.2, is centred at 0.6 THz and extends up to 3 THz.

A material that averts two-photon absorption of 800 nm pump light

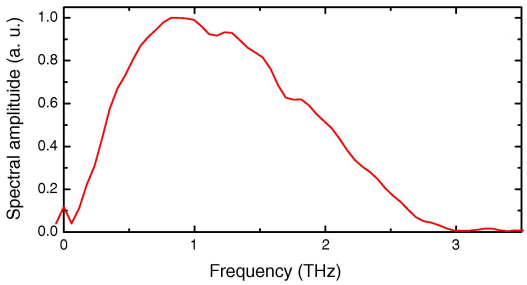

Figure 2.3: From [5]. Spectrum of the THz from LNO.

(and three-photon absorption of 1 μm pump wavelengths) is lithium niobate (LNO[1]). At the same time, LNO displays a relatively high effective nonlinear coefficient ($|d_{33}| = 27$ pm/V [16]), which we know to be crucial in ensuring high efficiency in the frequency conversion process. However, nonlinear optical crystals such as LNO and other ferroelectrics preclude the use of the *collinear* velocity matching geometry, since THz waves - which take the form of phonon-polariton waves in these materials - have phase velocities far too slow to match optical group velocities ($n_g = 2.25$ at 800 nm, while $n_{THz} = 4.96$ [21]). This is why they call for a sophisticated *non-collinear* pump configuration, consisting of diffraction gratings that tilt the pulse front, with the tilt angle adjusted to let the pump pulse reach the velocity matching with THz radiation. In this way, generation of THz pulses has been achieved in LNO, with a pump-to-THz *energy conversion efficiency* of 7 x 10^{-4}, starting from a laser pulse at 800 nm [5]. The spectrum is shown in Figure 2.3: it is centerd at 1 THz and extends up to 3 THz.

A comparison between the conversion efficiencies of LNO and ZnTe is reported in [11]. The two systems are both excited by a laser pulse at 1.03 μm, running at 1 kHz repetition rate. Tilted pulse-front excitation for LNO gives a conversion efficiency of 2.5 x 10^{-4}, that is more than one order of

[1] $LiNbO_3$.

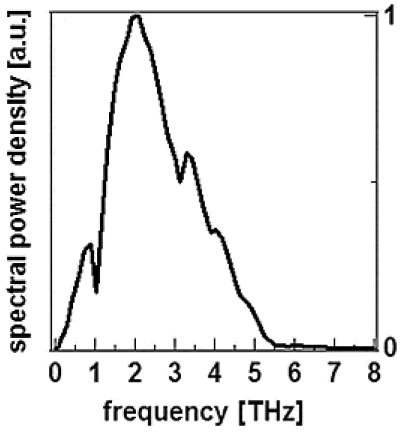

Figure 2.4: From [14]. THz spectrum from DAST pumped at 1.5 μm.

magnitude higher than both the one obtained with collinear OR in GaP, and with an optimized noncollinear geometry in ZnTe. In fact, in ZnTe and GaP, at high pulse energy, a strong saturation in the generated THz energy - that is attributed to two- and three-photon absorption in the respective materials - appears, whereas in LNO not. In LNO, a bandgap of 3.8 eV at room temperature [12], makes possible only four-photon absorption, when the pump wavelength is 1.03 μm.

2.2.2 High-field THz generation in organic crystals

It seems from the previous section that, when selecting a nonlinear crystal for THz generation, one has to make a choice between nonlinear crystals such as ZnTe and GaP, in which phase-matching can be reached in a *collinear* geometry, but that present a low *energy conversion efficiency*; and *high-dielectric ferroelectrics* such as LNO, that nevertheless require a *sophisticated pulse-front tilting scheme* for the approximate fulfilment of the phase-matching condition. This is only because, up to now, the organic crystals haven't been taken into consideration.

DAST[2] and DSTMS[3] indeed display an *extremely high* second order nonlinear optical susceptibility that can be exploited in a simple *collinear* generation scheme. The value of the component along the direction [111] of the effective nonlinear second order coefficient, d_{111}, in DSTMS and DAST is, respectively, 214 pm/V ([18]) and 210 pm/V ([17]), at 1.9 μm. The spectrum of a CEP-locked high power THz pulse, generated from a *collimated* infrared pump beam sent through a DAST crystal at normal incidence, is plotted in Figure 2.4 [14]. It covers a range of 0.1 - 5 THz, apart from an absorption line at 1.1 THz, that is due to the well-known transverse optical phonon mode in DAST. An *energy conversion efficiency* of 2.2% has been calculated. For different pump laser wavelenghts spanning from 1.2 to 1.5 μm, the temporal and spectral characteristics of the THz pulses generated appear almost identical.

It is interesting at this point to make a comparison between DSTMS and DAST. In DSTMS, the dominant resonance is shifted to a lower frequency (1.024 THz) with respect to the one in DAST. Furthermore, the absorption strength at this peak is only 235 cm^{-1}, compared to 420 cm^{-1} at the dominant resonance of DAST. This is why, in the plot in Figure 2.5 of $L_{max}(\omega)$ as a function of the pump wavelength and the THz frequency , the "valley" centered at the absorption line near 1 THz is much narrower for DSTMS. This practically means that the absorption peak at 1 THz is much less pronounced in DSTMS, so this crystal is preferable if one is interested in generating THz radiation in the region from 1 to 4-5 THz. Notice that the highest values for $L_{max}(\omega)$ are obtained for pump wavelengths between 1400 nm and 1700 nm for both materials.

By optimizing the pump wavefront curvature and the imaging system

[2] 4-N,Ndimethylamino- 40-N0-methyl stilbazolium tosylate.

[3] 4-N,N-dimethylamino-4'-N'-methyl-stilbazolium 2,4,6- trimethylbenzenesulfonate.

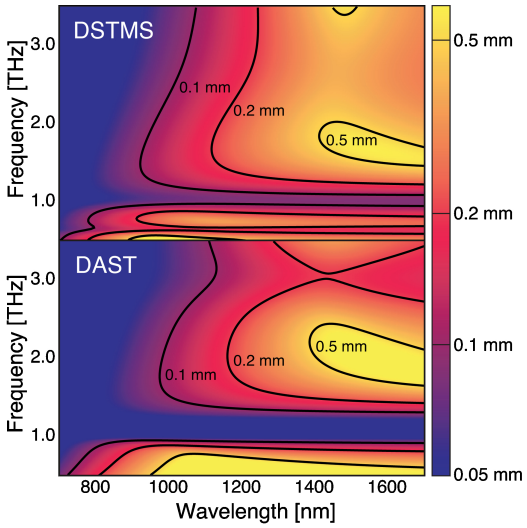

Figure 2.5: From [13]. Contour plots of the maximum effective length $L_{max}(\omega)$ as a function of the pump wavelength λ and the THz frequency ν. Top panel: DSTMS. Bottom panel: DAST. The "valley" at the phonon resonance near 1 THz is narrower and less pronounced for DSTMS, and $L_{max}(\omega)$ is more homogeneous than for DAST in the range of 1.5 to 3.5 THz.

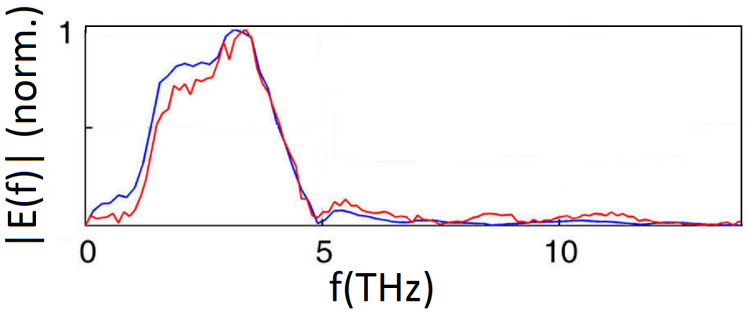

Figure 2.6: From [15]. Measured THz from DSTMS pumped at 1.5 μm. The blue curve shows the measurement using EOS. Air-biased coherent detection measurement is shown in red.

after THz generation, peak fields of around 80 MV/cm have been obtained in DSTMS in the spectral region 1 - 5 THz, as can be seen in Figure 2.6 [15].

2.3 Generation of MIR pulses via DFG

The output power of the MIR wave obtained by DFG in a suitable nonlinear crystal is given by the well-known formula [24] :

$$P_3 = \frac{2\omega_3^2 d_{eff}^2 L^2}{\epsilon_0 c^3 n_1 n_2 n_3} \frac{P_1 P_2}{\pi r^2} T_1 T_2 T_3 L_{eff},$$

$$L_{eff} = \exp(-\alpha_3 L) \frac{1 + \exp(-\Delta\alpha L) - 2\exp\left(-\frac{1}{2}\Delta\alpha L\right)\cos(\Delta k L)}{(\Delta k L)^2 + (\frac{1}{2}\Delta\alpha L)^2} \tag{2.7}$$

where P_1 and P_2 are the input peak powers of the two OPAs, and P_3 is the peak MIR generated. T_1,T_2, and T_3 are the respective single surface power transmission coefficients. $\Delta k = k_3 - k_2 - k_1$ is the momentum mismatch. α_1, α_2, and α_3 are the absorption coefficients at the respective frequencies, and $\Delta\alpha = |\alpha_3 - \alpha_2 - \alpha_1|$. L is the thickness of the crystal.

From equation 2.7, we see that, in order to evaluate the conversion efficiency from the two incident laser beams to the MIR wave, it is worth considering the figure of merit (FM) [1]:

$$FM = \frac{d_{eff}^2}{n_1 n_2 n_3} \tag{2.8}$$

where n_3, n_2, and n_1 are the refractive indices at pump, signal, and idler wavelengths, respectively.

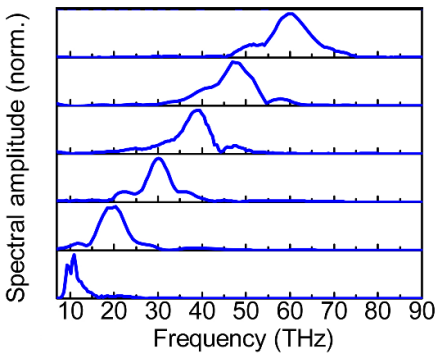

Figure 2.7: From [19]. Normalized amplitude spectra from GaSe for widely tuned center frequencies, generated by DFG of the signal waves of both OPAs.

2.3.1 GaSe

Compared with some of the crystals that have been considered up to now, e.g. the organic crystal DAST, GaSe has a FM value that is not extremely high [21]. However, it can exploit its natural *birefringence* and the relatively flatness of the refractive index dispersion in the MIR region we are interest in (from 16 THz to 23 THz) to achieve phase matching $\Delta k = 0$ at frequencies that can be chosen rather arbitrarily within that region. Furthermore, it presents an extended MIR transparency, from less than 10 THz up to 460 THz [1]. For all these reasons, it is widely used for the generation of MIR pulses through DFG.

GaSe soffers two-photon absorption when pumped at 800 nm due to the absorption onset at 0.65 μm; this is why, if the carrier frequency of the laser is at 800 nm, it requires a parametric setup to be pumped in the near-infrared (NIR). Peak fields up to 108 MV/cm and pulse energies as high as 19 μJ has been achieved with type-II DFG in this material [19]. The *photon conversion efficiency* $\eta_P = N_{MIR}/N_{NIR}$ has been calculated to be 14 %, a

value that exceeds the one obtained with OR of a single pulse by three orders of magnitude. This is because in DFG the full spectra of both OPA pulses contribute to the mixing process, while OR utilizes only the spectral wings. By varying the wavelength of one of the two OPAs between 1.1 μm and 1.5 μm, while keeping fixed the wavelength of the other at 1.1 μm, waveforms with carrier frequencies spanning from 10 to 72 THz has been generated (Figure 2.7).

2.4 Detection of THz and MIR pulses

The 4.1 mV energy of a 1 THz photon is smaller than the average kinetic energy of a free particle at room temperature (at 300 K, $k_B T \approx 25$ meV $\approx$ 6 THz). Semiconductor detectors - relying on the creation of a number of electron-hole pairs proportional to the energy of the radiation impinging on the device - can therefore not be used in the THz range at room temperature, and also thermal detectors would need operation at cryogenic temperatures (like bolometers for FTIR applications). The characterization of the THz pulses employed in this thesis was performed by means of *Electro-Optic (EO) sampling*. This is is an optoelectronic detection technique based on the *electro-optic effect*, that is the change in refractive index of a material, induced by the presence of a static or low-frequency (THz, in our case) electric field. With respect to *incoherent* intensity detection (like the one performed by using Si-bolometers), the *coherent* EO sampling technique enable the recovery of both the amplitude and the phase of the THz field. Furthermore, an EO sampling scheme works perfectly at room temperature.

2.4.1 Electro-optic sampling

In some materials, the change in refractive index depends linearly on the strength of the applied electric field E. This change is known as the *linear electro-optic effect* or *Pockels effect* [2]. Putting aside anisotropy effects:

$$\Delta n = n^3 r E \tag{2.9}$$

where r is the *electro-optic coefficient*. Let us see how, exploiting the Pockels effect, a direct measure of the electric field profile of a THz pulse is possible. In the following we will speak about THz pulses, but the electro-optic sampling technique has been used to characterize both THz and MIR pulses.

An *optical sampling pulse* co-propagate with the THz field through a nonlinear detection crystal. If the *THz phase velocity* and the *optical group velocity* match, the optical pulse - that must have a time duration much shorter than the one of the pump - feels a constant electric field, that is the instantaneous THz field. The polarisation of the optical probe is rotated by the birefringence induced by the pump. The degree of rotation is proportional to the THz field amplitude, so a measurement of the former gives the value of the THz electric field at the point the two pulses overlap. Scanning the delay between the THz and the optical pulse allows the recovery of the whole electric field profile of the THz pulse.

With the help of the EO scheme depicted in Figure 2.8, we can understand how the rotation of the probe polarisation is measured. After the nonlinear detection crystal, a half-wave ($\lambda/2$) plate and a Wallaston prism are placed. The optical pulse is splitted by the prism in two orthogonal-polarised pulses, that are then sent into a balanced photodetector, whose output signal is the difference between te outputs the two photodiodes. The $\lambda/2$ plate is aligned

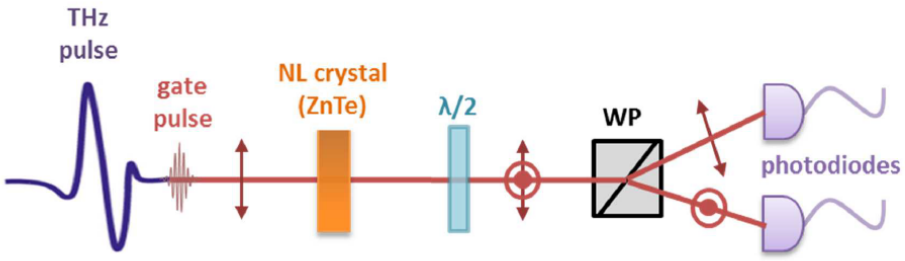

Figure 2.8: Electro-optic sampling scheme. $\lambda/2$: half-wave plate. WP: Wollaston prism.

in such a way that, in the absence of the THz field, the two orthogonal-polarised pulses have the same intensity, so that they give rise to a zero signal from the balanced photodetector. Only when the THz field overlaps with the sampling pulse inside the crystal, since the polarisation of the probe pulse is rotated, an intensity difference is measured between the two photodiodes, resulting in an output signal linearly proportional to the amplitude of the THz field. This procedure is very sensitive, allowing for the detection of THz pulses with less than 1 nJ energy.

The THz probe pulses used in our setup are generated through OR in a 0.5 mm thick (100) cut ZnTe crystal. The gate is an optical pulse at 800 nm, directly coming from the laser. The electro-optically active medium used is another 0.5 mm thick (110) cut ZnTe crystal, selected because it approximately satisfies the phase-matching condition between pulses at 800 nm and 0 to 5 THz, and because has a relatively large electro-optic coefficient. Its first TO phonon mode is at 5.3 THz, which restricts its detectable bandwidth to about 5 THz. For higher frequency investigations within the THz range, crystals such as GaP should be used. Typical THz transients obtained with this system are shown in figure 2.9.

To characterize the MIR frequency pulses - generated in our setup through

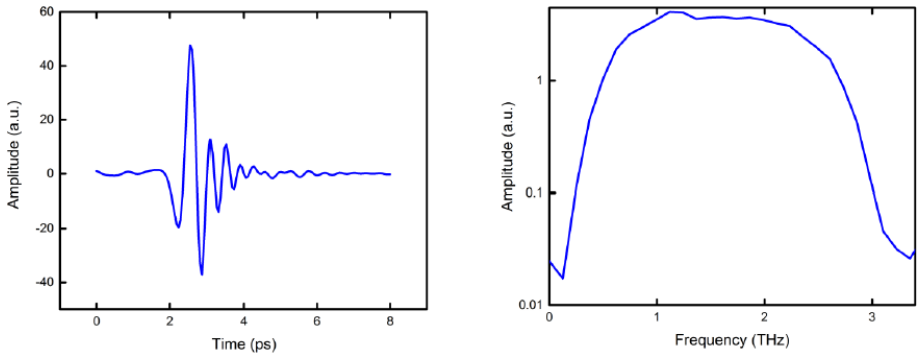

Figure 2.9: THz time-domain traces and associated spectra of the probe, from electro-optic sampling.

difference frequency interaction in 1 mm thick GaSe crystal -, another GaSe crystal ($50\mu m$ thick) is used as electro-optically active medium (see section 2.3.1). The gate in this case is a compressed optical pulse (800 nm) of 80 fs time duration.

2.5 CEP stability

The carrier envelope phase (CEP) of a laser pulse is the relative phase that the electric field profile has with respect to its envelope. Figure 2.10 shows two examples of pulses with the same envelope but different CEPs. A laser source is called CEP stable if all the generated pulses have the same CEP. Because time-resolved gating techniques like the EOS require scanning the THz-gate delay, the THz and MIR pulses employed need to be CEP stable, i.e. they must have a reproducible electric field profile. CEP stable pulses can be generated starting from non-CEP stable sources by exploiting the existing phase relations between the pulses involved in nonlinear optical processes like DFG.

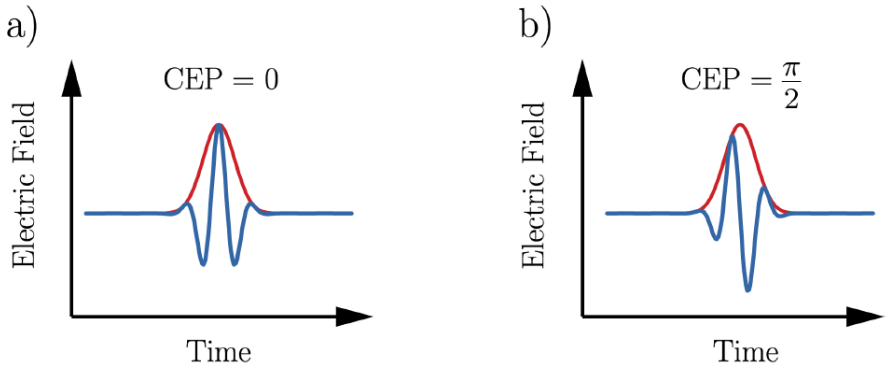

Figure 2.10: Example of pulses with the same intensity envelope (red line) but different CEPs.

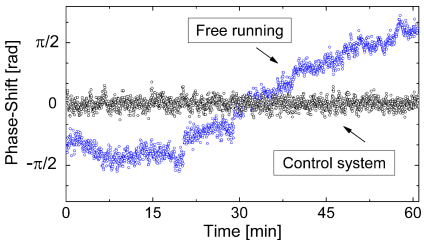

Figure 2.11: From [22]. Long-term characterization of the MIR phase drift. Both free-running and closed loop measurements are displayed.

Difference frequency (DF) mixing between pulses at different frequencies with carrier-envelope phases ϕ_1 and ϕ_2, generates a pulse with absolute phase given by ([23]):

$$\phi_{DF} = \phi_1 - \phi_2 - \pi/2 \tag{2.10}$$

When the two interacting waves are derived from the same source - i.e., the two pulses are generated by two OPAs that are seeded by the same white light - or are different components of a broadband pulse (OR), they are *mutually phase-locked* , and their phases can be written as $\phi_1 = \phi_2 + \Delta\phi$, with $\Delta\phi$ constant. The difference frequency process then generates, according to 2.10, a wave with phase $\Delta\phi - \pi/2$ that is stable. In practice, then,

DF-generated pulses always present a long-term drift in the CEP due to unavoidable differences in the paths of the two interacting beams, but there exists simple techniques useful to instantaneously correct such a drift. One of these consist in changing one of the two pump beam paths, by using a control loop system [22].

In Figure 2.11 is displayed the effect of such a system on the phase shift.

Chapter 3

Controlling bandwidth: from broadband to narrowband pulses

In this chapter, the experimental setup for the generation of *narrowband, tunable, high-energy, CEP-stable* MIR pulses is described. Emphasis is placed on *minimizing the bandwidth* and on the *frequency tunability*: pulses between 16 and 23 THz with a bandwidth of less than 0.8 THz (FWHM) were achieved through DFG in GaSe between two equally linearly chirped NIR pulses. Furthermore, if one is interested in generating lower frequency fields, it sufficient to substitute the GaSe crystal with a suitable crystal like DSTMS (pulses between 4 THz and 18 THz has been demonstrated in a similar setup [25]). We remark that such a tunability wouldn't have been possible with a generation method based on OR. The CEP stability is obtained by seeding the two identical optical parametric amplifiers (OPAs) that generate the two NIR pulses with the same wight light continuum: in this way pulses with correlated carrier-envelope phase fluctuations are generated, that are

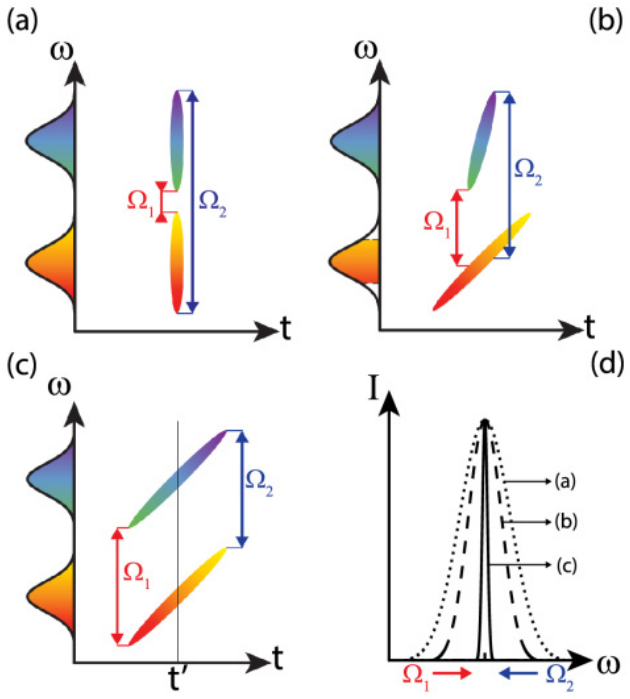

Figure 3.1: From [26]. Principle of the narrowband MIR generation. (a)-(c): time-frequency Wigner distributions of the interacting NIR pulses for various chirp configurations. The MIR components are generated at the DF between NIR spectral frequencies at the same time delay. Ω_1 and Ω_2 are the lowest and highest frequency generated during the whole interaction time, respectively. (d) Corresponding MIR spectra.

then subtracted in the DFG process, hence yielding a stable carrier-envelope phase of the MIR pulse, making it possible to measure its electric field by EOS (see section 2.5).

3.1 Narrowband MIR pulse generation: principles

Figure 3.1 summarizes the principle of narrowband MIR pulse generation through DFG among linearly chirped pulses. According to energy conserva-

tion, the MIR light is generated at the difference frequency of the two frequency components that interact at the same time in the nonlinear medium. The MIR bandwidth can be estimated at the zero order as $\Delta\Omega = \Omega_2 - \Omega_1$, where Ω_1 (Ω_2) is the lowest (highest) frequency generated during the whole interaction time. If the two NIR pulses are *Fourier-transform limited* - i.e. for a certain bandwidth the pulse duration is the shortest possible - all the frequencies of the two NIR pulses interact at the same time [see Figure 3.1 (a)], giving rise to the broadest MIR pulse [dotted line in Figure 3.1 (d)]. If the two NIR pulses are *linearly chirped* - i.e. the instantaneous frequency $\omega(t)$ can be written as $\omega(t) = \omega_0 + \beta t$, with ω_0 being the central frequency and β the *linear chirp* - with different group delay dispersion (GDD), as depicted in Figure 3.1 (b), only a subset of their frequency components can interact, leading to a decrease in the MIR bandwidth [dashed line in Figure 3.1 (d)]. The two NIR chirped pulses can be described as $E_i(t) = E_{0i}(t)\exp[i(\omega_i t) + \beta_i t^2]$, where $E_{0i}(t)$ is the envelope and give rise to MIR pulses $E_{MIR}(t) = E^*_{01}(t)E_{02}(t)\exp[i(\omega_1 - \omega_2)t + i(\beta_1 - \beta_2)t^2]$. Since the chirp in the two pulses is different, $\beta_1 \neq \beta_2$, the MIR pulses acquire a time-dependent frequency,i.e., they are also chirped. furthermore, if the two NIR pulses have the same bandwidths, this also implies that some of the frequency components of the most dispersed pulse do not interact with the other pulse, resulting in a strong reduction of the DFG efficiency. If the two NIR pulses are chirped with the same amount of GDD [see Figure 3.1 (c)] $\Delta\Omega = \Omega_2 - \Omega_1 \approx 0$. This leads to the generation of the narrowest, in principle unchirped ($\beta_1 - \beta_2 = 0$) MIR pulse. Actually, the DF spectrum gets inevitably broadened, since at any time t' in the Wigner map in Figure 3.1 (c) each one of the two NIR has a bandwidth different from zero. To control the bandwidth of the MIR [solid line in figure 3.1 (d)] on can refer

to the fact that the MIR, according to what we deduced from the formula, is unchirped; so, its bandwidth is inversely proportional to its time duration, whose cannot be longer than the one of the interacting NIR pulses. So, the longer the pulse duration of the stretched NIR, the narrower the bandwidth of the DF generated MIR.

3.2 Experimental setup

Figure 3.2 displays a schematic drawing of the optical setup. A commercial Ti: sapphire regenerative amplifier, delivering 800 nm wavelength pulses of 7 mJ energy and 80 fs duration (FWHM) at 1 kHz repetition rate was used to pump two identical three-stage optical parametric amplifiers (OPAs). OPA1 and OPA2 generated 1.38 μm and 1.55 μm wavelengths beams, respectively, that were sent to two identical stretchers (S1 and S2 in Figure), that introduced the same amount of dispersion to the two beams. The two equally linearly chirped pulses met in the GaSe nonlinearcrystal, where generated MIR pulses with wavelength between 13 and 17 μm through difference frequency generation.

3.2.1 The optical parametric amplifiers (OPAs)

The sources of femtosecond pulses, like the laser used in our setup, operate at fixed wavelengths. However the need to excite a system on resonance requires broad frequency tunability: this is achieved by the *optical parametric amplification* (OPA) nonlinear process. In a suitable non linear crystal, energy is transferred from the high frequency and high energy beam directly coming from the laser (the *pump beam* at frequency ω_3) to a lower frequency, lower intensity beam (the *signal beam* at frequency $\omega_1 < \omega_3$) which is thus

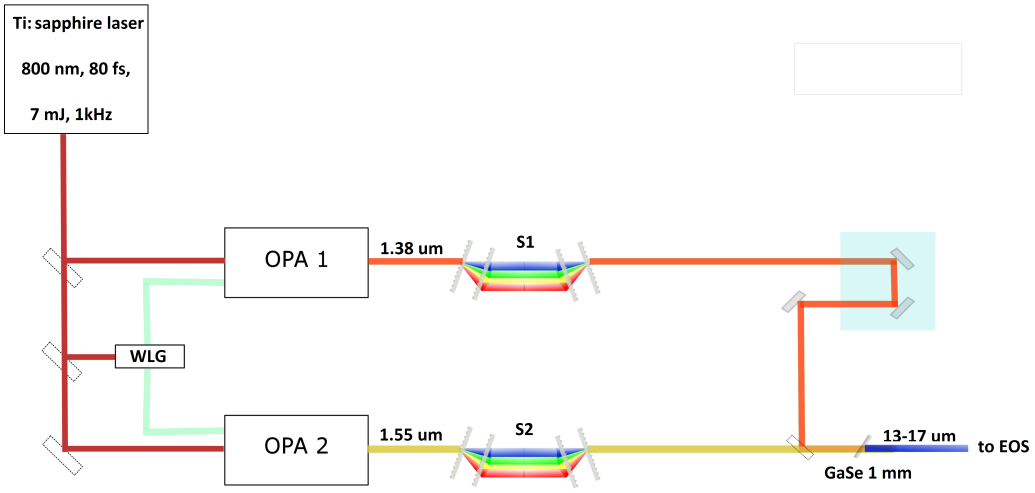

Figure 3.2: Setup for the generation of narrowband MIR pulses. OPA I and II: three-stage OPAs; WLG: white light generation; S_1 and S_2: stretchers. A commercial Ti: sapphire regenerative amplifier, delivering 800 nm wavelength pulses of 7 mJ energy and 80 fs duration (FWHM) at 1 kHz repetition rate was used to pump two identical three-stage optical parametric amplifiers (OPAs). OPA1 and OPA2 generated 1.38 μm and 1.55 μm wavelengths beams, respectively, that were sent to two identical stretchers (S1 and S2 in Figure), that introduced the same amount of dispersion to the two beams. The two equally linearly chirped pulses met in the GaSe nonlinearcrystal, where generated MIR pulses with wavelength between 13 and 17 μm through difference frequency generation.

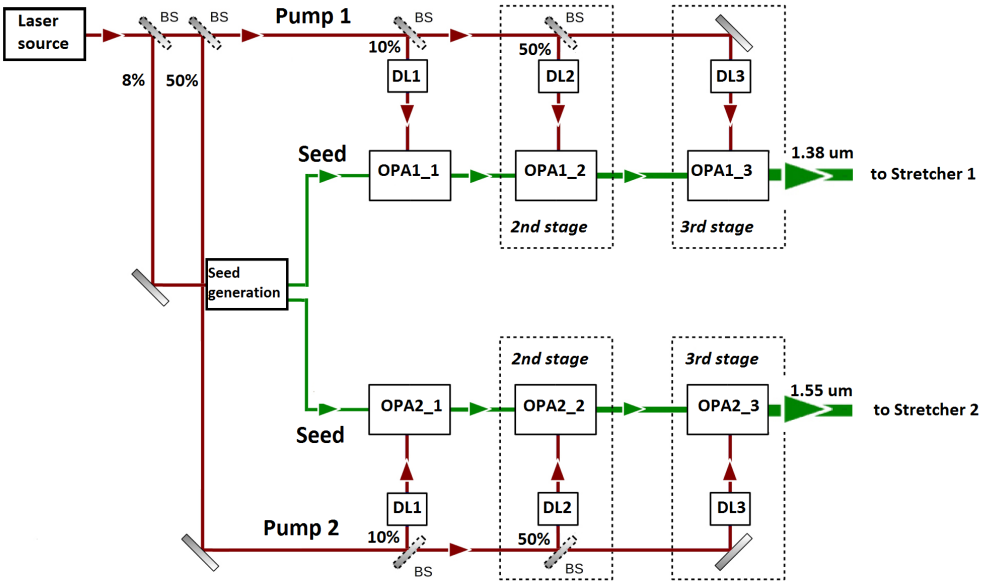

Figure 3.3: Schematic of the two OPAs used in the experiment. BS: beam splitter. DL: delay stage. Part of the beam coming from the Ti:sapphire laser is used to generate wight light pulses in Sapphire plate. The wight light is split into two parts and is sent to the two OPAs. Here, the parametric amplification process takes place in 2.5 mm and 3 mm thick BBO crystals pumped by the remaining part of the initial beam. The two OPAs are identical, except for the fact that the respectively BBO crystal are slightly differently rotated such that one generates 1.38 μm wavelength pulses, while the other 1.55μm. Both the OPAs generete pulses with maximum energy of 850 μJ. Hence, their *photon conversion efficiency* is around 42 and 47 % respectively.

amplified. The frequency of the *signal* at which the *pump* transfers energy is determined by the phase-matching condition. By rotating the nonlinear crystal in a proper way, the phase-matching condition is fulfilled for *signals* at different frequencies: in this way, the desired frequency tunability is achieved. OPA is nothing but a DFG mechanism; the only difference stays in the strength of the interacting fields: DFG arise when the pump and the signal fields have comparable intensities, while OPA occurs when the signal is much weaker.

In Figure 3.3 it is depicted a schematic of the two OPAs used in our setup. A small fraction of the 7 mJ pump beam coming from the Ti:sapphire laser is used to generate wight light pulses, focussed in sapphire. The wight light is split into two parts and is sent to the two OPAs. The pump pulses are s-polarized and type-II phase matching in Beta Barium Borate (β BBO) is used to select in the first stage the signal wavelengths of 1.38 and 1.55 μm for amplification from the continuum. Pumped with 322 μJ pulses, signals with energies of around 30 μJ are generated, which are then used to seed the next two amplification stages (see the Figure for details on the beam distribution into each OPA). At the end, pulses with maximum energy of 700 and 650 μJ are generated at 1.38 and 1.55 μm. This corresponds to an overall *photon conversion efficiency* value of 42 and 43 %, respectively. We decided to tune the two OPAs to 1.38 and 1.55 μm (we are obviously referring to the *signals*) because the modes we were interested in exciting lie below 23 THz and because in that frequency range it is guaranteed a high *efficiency transmission* of the stretcher's gratings. The duration of the high energy pulses is around 90 fs. They are focused onto the gallium selinide (GaSe) crystal almost collinearly to generate the MIR pulses, yielding 7-8 μJ pulse energy at 13 μm. Te overall photon conversion efficiency of the

conversion is thus approximately 1.9 %.

3.2.2 The stretcher

When a laser pulse is *transform limited*, each frequency arrives at the sample at the same time; equivalently, its time duration is the shortest one permitted by a given bandwidth. When, within the spectrum of a transform limited pulse, some frequencies are delayed with respect to others, the pulse is *stretched*: its time duration is increased. A stretched pulse can be compressed, if the delayed frequencies are made to travel over a shorter path than the other wavelength components of the beam; a transform limited pulse cannot. The phenomenon of delaying or advancing some wavelenths relative to others is called *group delay dispersion* (GDD) or, less formally, *chirp*. A pulse is said to be *positively chirped* when the longer wavelengths lead the shorter wavelengths. Conversely, if the redder light is delayed more than the bluer light, it has a *negative chirp*. Stretchers and compressors are dispersive optical elements that introduce a certain amount of positive or negative GDD to the beam. To understand the meaning of this quantity it is worth recalling some important concepts from linear optics.

The physical meaning of the GDD

For ultrashort pulses, the electric field $E(z,t)$ is frequently written in terms of a slowly varying envelope $B(z,t)$ times a travelling optical carrier term $cos(\omega_0 t - k_0 z + \phi(t))$ at frequency ω_0 and time-dependent phase $\phi(t)$ [1]:

$$E(z,t) = B(z,t)cos(\omega_0 t - k_0 z + \phi(t)) = \mathrm{Re}\{B(z,t)\exp(j(\omega_0 t - k_0 z + \phi(t)))\} \tag{3.1}$$

We usually call $A(z,t) = B(z,t)\exp[j\phi(t)]$. For simplicity, the z dependence of the electric field is neglected in the following.

An electric field can be described also in the frequency domain; thanks to the fourier-transform operator, it is possible to switch from the time domain to the frequency domain:

$$\tilde{E}(\omega) = \mathscr{F}(E(t)) = \frac{1}{\sqrt{2\pi}} \int_{-\infty}^{+\infty} E(t)\exp(-j\omega t)dt. \tag{3.2}$$

Viceversa,

$$E(t) = \mathscr{F}^{-1}(\tilde{E}(\omega)) = \frac{1}{\sqrt{2\pi}} \int_{-\infty}^{+\infty} \tilde{E}(\omega)\exp(j\omega t)d\omega \tag{3.3}$$

is the inverse Fourier transform. Equation 3.3 shows that $E(t)$ can be seen as a superposition of an infinite number of monochromatic light waves with angular frequency ω. $\tilde{E}(\omega)$ in equation 3.2 is the complex coefficient of each monochromatic wave, and can be decomposed in:

$$\tilde{E}(\omega) = |\tilde{E}(\omega)|\exp(j\Phi(\omega)) \tag{3.4}$$

where $|\tilde{E}(\omega)|^2$ is the *spectrum* of the wave, and $\Phi(\omega)$ is its *spectral phase*.

In a medium that is *dispersive* (i.e., $n = n(\omega)$, with n being its refractive index) and *linear* (i.e, the applied electric field id sufficiently low that one can write $P_{NL} = 0$), each one of the monochromatic waves with angular frequency ω and wave vector $k(\omega) = \frac{\omega}{c}n(\omega)$ that constitute the propagating pulse travels with a velocity $\frac{c}{n(\omega)}$. The quantity

$$\Phi(\omega) = k(\omega)z = \frac{\omega z}{c/n(\omega)} \tag{3.5}$$

is the spectral phase accumulated by each monochromatic wave after

having propagated for a distance z through the dispersive linear medium. Notice that $\Phi(\omega)/\omega$ is the time that a monochromatic wave took to travel along such a distance.

Let us approximate the spectral phase with a Taylor expansion around the pulse carrier frequency ω_0:

$$\Phi(\omega) = \Phi(\omega_0) + \frac{\partial\Phi(\omega)}{\partial\omega}|_{\omega_0}(\omega - \omega_0) + \frac{1}{2}\frac{\partial^2\Phi(\omega)}{\partial\omega^2}|_{\omega_0}(\omega - \omega_0)^2 + \dots \quad (3.6)$$

If we stop at the first order in that expansion and substitute the resulting expression for $\Phi(\omega)$ in the equation 2.3 (where now the RHS is zero), we find that each one of the monochromatic components that constitute the progressive wave is moving through the medium with the same velocity (that is the so-called group velocity $v_g = \frac{\partial\omega}{\partial k}|_{\omega_0}$). The only difference with respect to a wavepacket propagating in vacuum is that the velocity of each monochromatic component at ω is v_g and not c. Obviously, v_g is always lower or at maximum equal to c; this means that the wave-packet accumulates -during the propagation through the dispersive medium- a time delay with respect to a wave-packet in vacuum. Such time-delay is

$$GD(\omega_0) = \frac{\partial\Phi(\omega)}{\partial\omega}|_{\omega_0} = z\frac{\partial k}{\partial\omega}|_{\omega_0} \quad (3.7)$$

and is called *group delay* (GD). The remarkably thing is that within this approximation (first order expansion of $\Phi(\omega)$) there is no dispersion of the wave-packet during the propagation through the *dispersive* medium.

But we know that there must be dispersion because the velocity of propagation $\frac{c}{n(\omega)}$ is different for at least two monochromatic components ω, since $n(\omega)$ cannot be constant for all the frequencies, otherwise the medium wouldn't

be dispersive. So, it makes sense to extend the expansion of $\Phi(\omega)$ at the second order (see equation 3.6), or equivalently to expand the GD at the first order:

$$GD(\omega) = GD(\omega_0) + GDD(\omega_0)(\omega - \omega_0) + \dots \tag{3.8}$$

where GDD is called *group delay dispersion*. From equation 3.6 it is evident that

$$GDD(\omega_0) = \frac{\partial^2 \Phi(\omega)}{\partial \omega^2}|_{\omega_0} = z\frac{\partial^2 k}{\partial \omega^2}|_{\omega_0}. \tag{3.9}$$

The higher is the GDD value (usually expressed in fs^2) for a given length z, the higher is the pulse broadening in time.

One can, at this point, expand equation 3.6 at the third order (or equivalently equation 3.8 at the second order). In this case, the quantity TOD - called *third order dispersion*- appears and is defined as $TOD(\omega_0) = \frac{\partial^3 \Phi(\omega)}{\partial \omega^3}|_{\omega_0}$. A strong TOD value, for a given length z, gives rise to an asymmetric temporal profile of the pulse and multiple delayed replica.

Let us now calculate the temporal profile of a gaussian pulse, written in the form

$$E(t) = \mathrm{Re}\left\{ A_0 \exp\left(-\frac{t^2}{2\tau^2}\right) \exp(j\omega_0 t)\right\}, \tag{3.10}$$

resulting from pure second order dispersion (i.e., we don't consider higher order in the expansion 3.6). After propagation in the dispersive medium, the pulse is still gaussian with a pulse duration τ_{out} (FWHM) that is given by

$$\tau_{out} = \tau_{IN}\sqrt{1 + (\frac{GDD(\omega_0)}{\tau_{IN}})^2} \tag{3.11}$$

where τ_{IN} is the pulse duration (FWHM) before the medium. this equation shows the main effect of GDD on the pulse width. When $GDD \ll \tau_{IN}^2$ (small dispersion with respect to the initial time duration of the pulse), $\tau_{out} \approx \tau_{IN}$: the pulse shape is almost unaffected by the presence of the medium. In contrast, when $GDD \gg \tau_{IN}^2$ (large dispersion with respect to the initial time duration of the pulse):

$$\tau_{out} \approx \frac{GDD(\omega_0)}{\tau_{IN}} \tag{3.12}$$

It means that the shorter is the pulse duration τ_{IN} the more the pulse is susceptible to dispersion broadening; the amount of broadening is proportional to the GDD value at the central frequency of the pulse ω_0. This can be intuitively understood by considering that a short pulse contains many frequencies which travel with different group velocities in the medium.

Dispersive stretcher with transmission grating pairs

In Figure 3.4 the stretcher that has been used in the experiment is schematically represented. It is based on two pairs of parallel gratings. The pulse coming from the OPA, incident on the first grating, is separated into its component wavelengths. The different wavelengths of the beam propagate along different directions in the space between the two gratings. After diffraction by the second grating, the beams of different wavelengths become parallel but they are separated in space. To make the beam to assume the same shape it had before the stretcher, a second grating pair, identical but rotated 90° right with respect to the first one, is placed. After the stretcher, the longer wavelength components of the incoming beam have traversed longer distance in comparison to the shorter ones. Thus pulses at higher frequencies arrive earlier than lower frequency pulses, in case of an incoming transform-

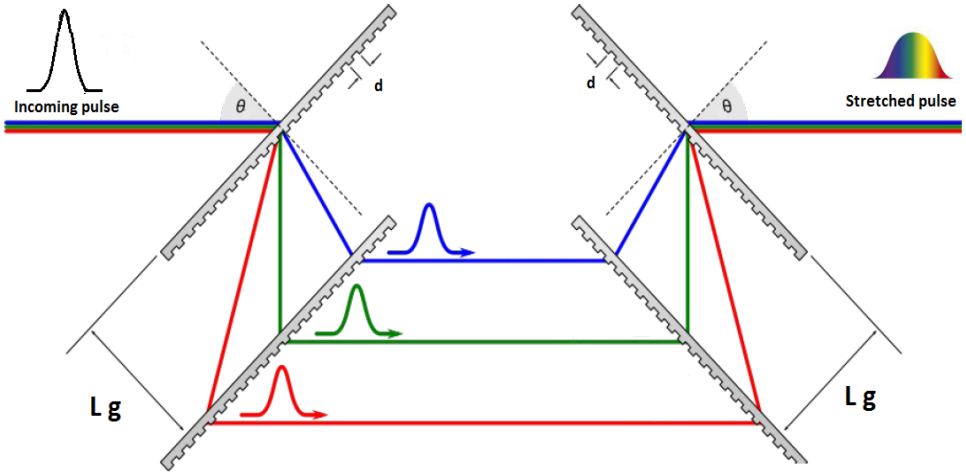

Figure 3.4: Schematic representation of the stretcher used in the experiment. It is made by two transmission grating pairs. The total amount of negative dispersion introduced by the stretcher is proportional to the distance L_g between the gratings that constitute a pair and it is two times the one introduced by a single grating pair.

limited pulse. This stretcher introduces a negative GDD. The total amount of negative dispersion is two times the one introduced by the first grating pair, that is given by the formula:

$$GDD(\omega_0) = -\frac{4m^2\pi^2 c\Lambda^2}{\omega_0^3}[1-(-m\frac{2\pi c}{\omega_0\Lambda}-\sin(\theta_i))^2]^{-3/2}L_g \qquad (3.13)$$

where: m is the order of diffraction; ω_0 is the central angular frequency of the wave-packet; Λ is the period of the grating; θ_i is the angle of incidence on the first grating; and L_g is the distance between the gratings that constitute a pair. What is remarkable is that, according to Formula 3.13, the total negative dispersion introduced by the stretcher is proportional to L_g, so it can be finely tuned simply by changing the distance between parallel gratings.

In the experiment, high-efficiency transmission gratings (almost 95% diffraction efficiency between 1.4 μm and 1.55 μm) with 966.2 lines/mm and an

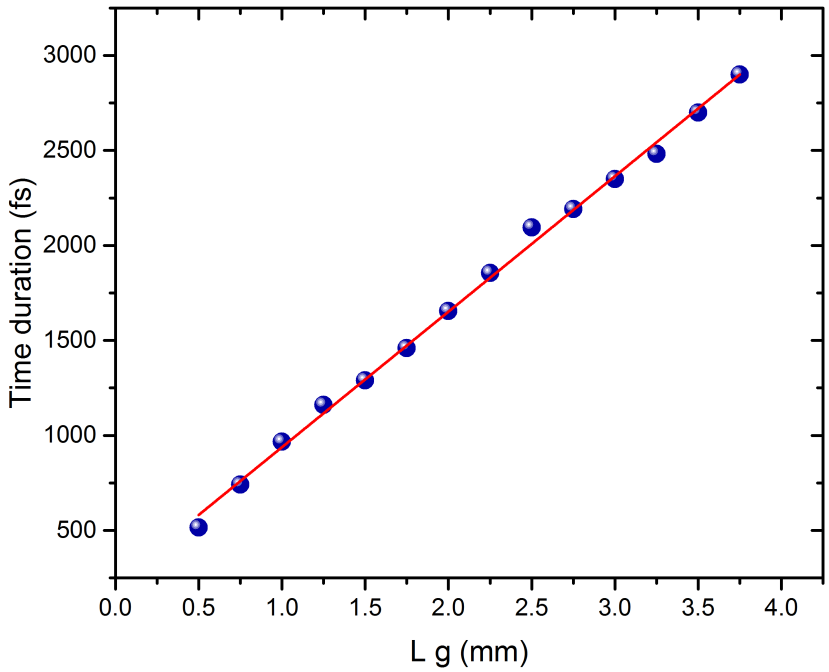

Figure 3.5: Time duration of the NIR beam after the stretcher as a function of the distance L_g between the gratings that constitute a pair, together with the linear fit (red line). The data come from FROG measurements. The maximum time duration achieved is 3 ps.

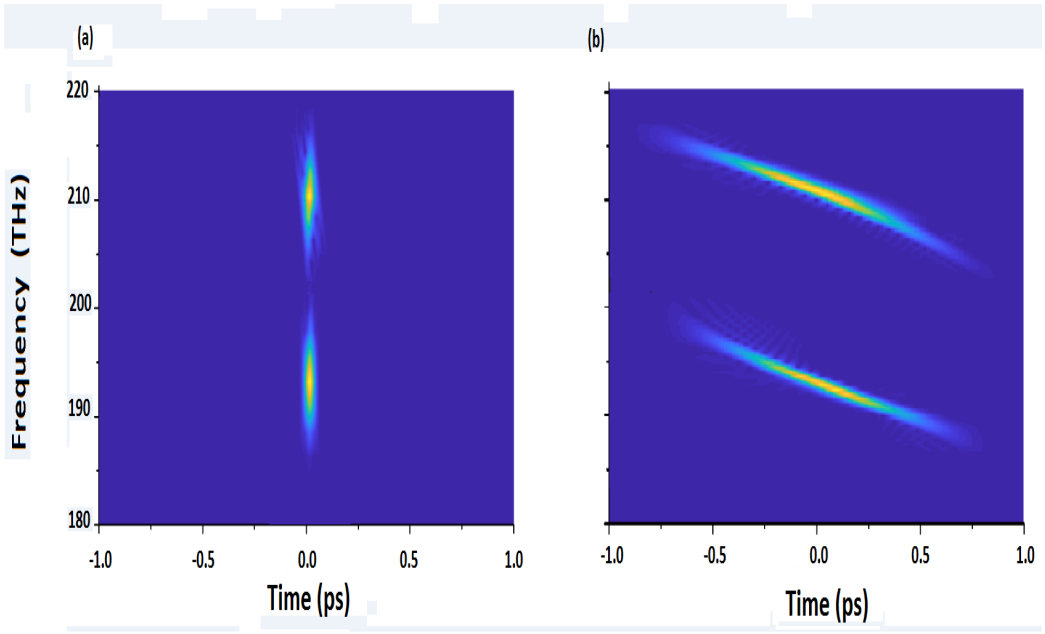

Figure 3.6: Time-frequency Wigner map of the NIR pulses before (a) and after (b) the stretcher, retrieved from frequency-resolved optical grating (FROG). Before the stretcher, both the NIR pulses had a time duration 90 fs (FWHM). After the stretcher, both are 780 fs long (FWHM). By correctly tuning the distance L_g between the gratings of the two stretchers, the time-frequency traces of the two pulses after the stretcher are parallel to each other. This is the situation shown in Figure 3.1 (c), that leads to the narrowest band MIR difference-frequency generated pulse.

angle of incidence θ_i of 48.3° have been used. By considering that m is equal to -1 and 1.55 μm as the wavelength of the incoming beam - for a minimum value of L_g equal to 500μm - we find from equation 3.13 a GDD value of 24 000 fs^2, that is consistent with the one obtained with the FROG measurement. Furthermore, the time duration τ_{IN} is 90 fs (from FROG measurement); this means that the minimum GDD value introduced by the stretcher in our setup (the one associated with minimum distance L_g between gratings) is already much bigger than τ_{IN}^2. So, in all the operating conditions we are in the case $GDD \gg \tau_{IN}^2$. This means, according to equation 3.12, that τ_{out} is linearly proportional to GDD. But the stretcher that has been used it holds that GDD is linearly proportional to L_g (equation 3.13). Putting equation 3.12 and 3.13, one expects that the time duration of the pulse after the stretcher is linearly proportional to L_g. This is indeed what we found from FROG measurement (see Figure 3.5). We managed to stretch the laser pulse up to 3 ps.

In our setup, two identical pulse stretcher were used to introduce equivalent amounts of negative linear chirp to the NIR pulses at wavelengths 1.42 μm and 1.55μm coming from the two OPAs. Figure 3.6 shows their time-frequency traces retreived from FROG measurements, before (a) and after (b) the stretcher. It can be seen that the central frequency of the two beams is not shifted by the stretcher. Before the stretcher, both the NIR pulses had a time duration 90 fs (FWHM). After the stretcher, both are 780 fs long (FWHM). By correctly tuning the distance L_g between the gratings of the two stretchers, the time-frequency traces of the two pulses after the stretcher are parallel to each other. This is the situation shown in Figure 3.1 (c), that leads to the narrowest band MIR difference-frequency generated pulse.

3.2.3 DFG between linearly chirped NIR pulses

The two OPAs in Figure 3.2 were tuned between 1.38 μm and 1.55 μm, so the laser pulses generated through DF could in principle have a carrier frequency ranging from a few THz to 23 THz. In practice, then, the lower frequency limit is set by the *Reststrahlen absorpion band* of GaSe at almost 16 THz. High-energy ($8\mu J$), narrowband, CEP stable, tunable between 16 THz and 23 THz pulses were generated through difference frequency interaction between equally linearly chirped pulses in 1 mm thick GaSe crystal (type II phase-matching). Notice that the NIR wavelengths were tuned to above 1.2 μm to prevent two-photon absorption in GaSe (see Section 2.3.1). The pulse energy for optimum time delay between the two NIR is around $8\mu J$. It was measured by a commercial thermopile detector. The MIR beam diameter in the focus was estimated to be around 230 μm. This value was obtained by measuring through a calibrated $300\mu m$ pinhole and was consistent for all the measurements, indicating that the beam quality was not affected by the NIR stretching setup. The resulting peak of the electric fiels is 3.3 $\frac{MV}{cm}$ ($Epeak = \sqrt{\frac{2Z_0 W_{pulse}}{A_{pulse}\tau_{MIR}}}$, where: Z_0 is the vacuum impedance; W_{pulse}, A_{pulse}, and τ_{MIR} are, respectively, the energy, the area and the duration of the MIR pulse). The energy of the mid-infrared pulses around 8 μJ can be kept constant even for the different pulse durations by adjusting the spot sizes in the GaSe nonlinear to maintain the gain coefficient. Three gold mirrors (two of them parabolic and the other one round) were used to first collimate and then focus the MIR onto the sample. Each of them has a reflectance of 97% in the frequency range of the MIR generated pulse. Taking into account also the CsI window, the pump fluence on the sample is lowered by a factor 0.22 ($1-0.97^3*0.85$) with respect to the value assumed after the GaSe generation crystal (11 $\frac{mJ}{cm^2}$). In conclusion, the *pump fluence* on the sample is around

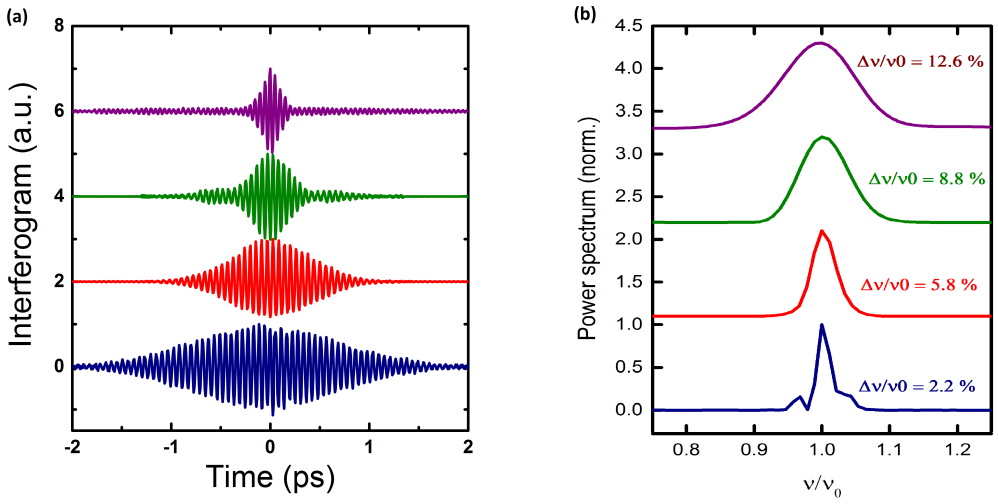

Figure 3.7: FTIR measurements for different distances L_g between the gratings of the stretcher. Only the first trace, the one with the largest relative bandwidth, comes from DFG between the two NIR beams that come directly from the two OPAs, without passing through the stretcher.(a): Interferograms as a function of the time delay between the two beams in which is split the MIR beam in the two arms of the interferometer. (b): corresponding relative bandwidth $\Delta\nu/\nu_0$ (FWHM) of the pulses. As the distance between the gratings increases, the time duration of the two NIR increases, and the relative bandwidth decreases.

8.5 $\frac{mJ}{cm^2}$.

In Figure 3.7, the *Fourier-transform infrared spectroscopy* (FTIR) measurements for different distances L_g between the gratings of the stretcher are displayed, together with the relative bandwidth $\frac{\Delta\nu}{\nu_0}$ of the pulses. Only the first trace, the one with the largest relative bandwidth, comes from DFG between the two NIR beams that come directly from the two OPAs, without passing through the stretcher.

The CEP stable MIR fields were then transmitted through a CsI window and characterized by EOS in a 50 μm thick GaSe crystal (see section 2.3.1). For this purpose, 40 fs gating pulses were obtained by compression of a low energy replica of the fundamental 800 nm beam, by using a sapphire crystal

and a prism compressor. The 2 mm thick CsI window was used in order to block low-frequency (and low-energy) THZ pulses generated due to OR in GaSe. In the frequency range we are interested in, it has 85% transmittance.

The EOS traces - obtained for difference distances between the gratings of the two stretchers (see Figure 3.8 (a)) -allowed us to retrieve the pulse duration of the MIR pulses. These values were compared with the ones obtained by considering the FWHM intensity of the pulse generated in the same setup of the EOS by sum-frequency between the 800 nm gate and the MIR pulses. As can be seen in Figure 3.8 (b), the two results were absolutely consistent. This allowed us to show in Figure 3.9 the intensity traces of the sum-frequency generated pulses, rather than the EOS traces, since they convey more clearly the information about the pulse duration.

At this point we had, for the different values of the distance between the gratings, both the time duration and the relative bandwidth of the pulses generated by difference frequency in GaSe. We had demonstrated in section 3.2.2 that, by increasing L_g, the time duration of the NIR pulses is increased proportionally, and consequently the time duration of the MIR ones. This implies - according to the discussion in Section 3.1- a linearly proportional reduction of the DF generated pulse bandwidth, since we expect that they are almost Fourier transform-limited. This is exactly what Figure 3.10 shows: the relative bandwidth (FWHM) of the MIR pulses decreases linearly as the time duration of the two NIR increases.

To check if the pulses are really almost transform-limited, we shown in table 3.2.3 the Transform-limited time duration calculated for the different positions of the gratings (except for the first value, that comes from DFG between the two NIR beams that didn't passed through the gratings of the

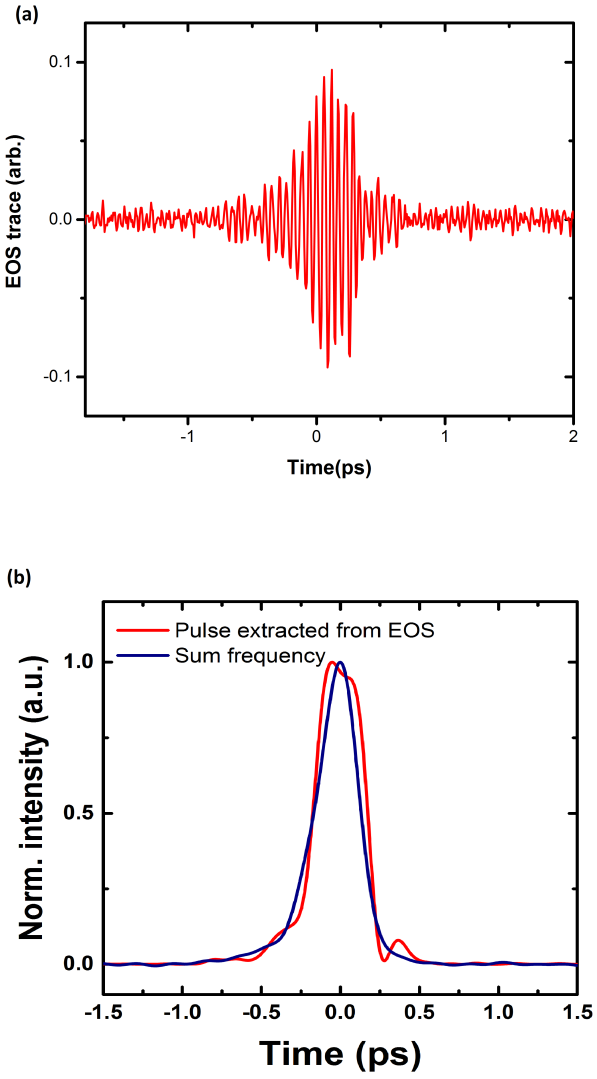

Figure 3.8: (a) EOS trace of a CEP stable MIR pulse. (b): the intensity of the pulse extraced from the electro-optic sampling has been compared with the intensity of the beam generated by sum-frequency between the MIR pulse and the 800 nm gate pulse. The two measurements are consistent.

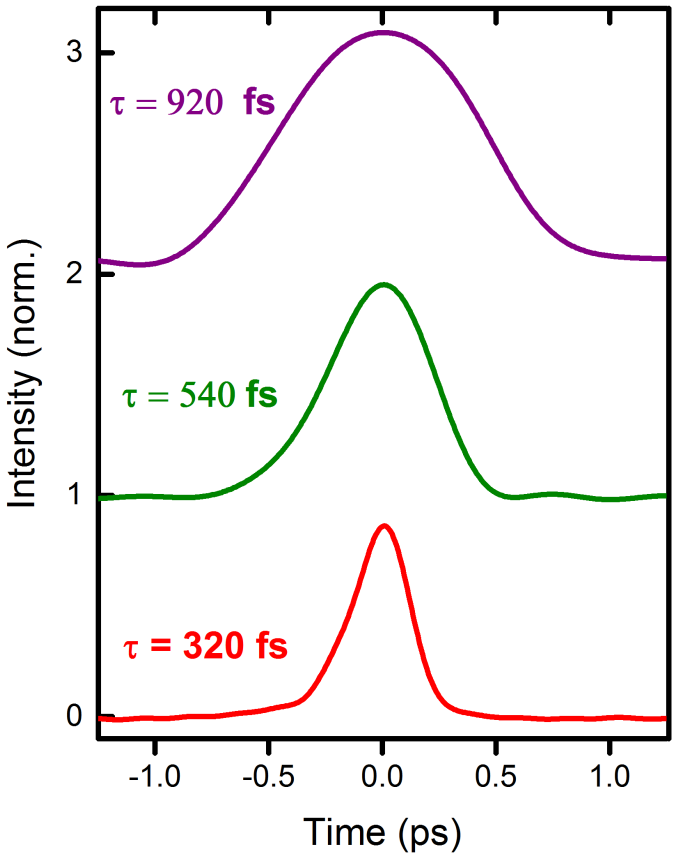

Figure 3.9: Time intensities of the beams generated by sum-frequency between the MIR pulse and the 800 nm gate pulse, for different positions of the gratings of the two stretchers. As the distance between the gratings increases, the time duration of the MIR DF generated pulses increases.

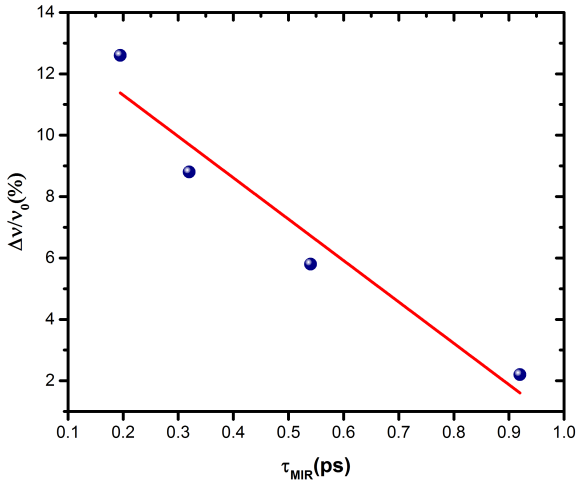

Figure 3.10: Relative bandwidth of the MIR pulses as a function of their time duration. As we expected from the discussion in Section 3.1, the relative bandwidth of the pulses decreases linearly with their time duration, since they are nearly transform-limited.

stretcher), by assuming a Gaussian pulse and by considering the bandwidth as extracted from the FTIR measurements. By comparing these values with the one measured with the EOS, we found that the time duration of the MIR pulses is always close to the transform-limited value (within 10 %).

Table 3.1: First column: bandwidths (FWHM) of the MIR pulses for the different positions of the stretchers as extracted from the FTIR measurements. Second column: time duration of the MIR pulses extracted from the time intensity of the pulses generated due to sum-frequency between the MIR and the 800 nm gate pulses. Third column: transform-limited time durations calculated by assuming Gaussian pulses and by considering the bandwidths values from the First column. Notice thast the first value comes from DFG between the two NIR beams that didn't passed through the gratings of the stretcher.

$FWHM(THz)$	$\tau_{MIR}(ps)$	$TL\tau_{MIR}(ps)$
2.5	0.195	0.176
1.6	0.32	0.275
0.97	0.54	0.45
0.39	1.12	0.92

3.2.4 Frequency tunability

In Figure 3.2 it is represented the delay stage, that is used to tune the temporal overlap between the two linearly chirped NIR pulses that come from the two stretchers. If the delay between the NIR pulses is changed, the subset of frequencies that can interact at any time t' in the DFG is shifted and so their difference frequency Ω_{MIR} changes (see the difference between Figure 3.11 (a) and (b)). In Figure 3.11 (c) is shown that the output MIR central frequency varies linearly with the delay between the incoming pulses.

In addition, the pulse energy of the narrowband MIR light scales with the shape of the gaussian spectrum of the two interacting NIR pulses, as can be seen in Figure 3.12 (d). This can easily be understood by looking at Figures 3.12 (a)-(c): when the time delay is zero [Figure 3.12 (b)] all the frequency components of one NIR pulse interact with all the others of the second NIR pulse, hence resulting in a huge transfer of energy to the generated MIR beam. In contrast, when the time delay is negative or positive, the interaction is only between the lowest frequencies of one of the two NIR and the highest frequencies of the others [Figure 3.12 (a) and (c)]. Data plotted in Figure (d) show that when the time delay between the two NIR is shifted such that the MIR central frequency is 1.5 THz different from the value given by the difference between the central frequencies of the two interacting NIR pulses, the MIR pulse energy decreases by 50%. This is why to tune the

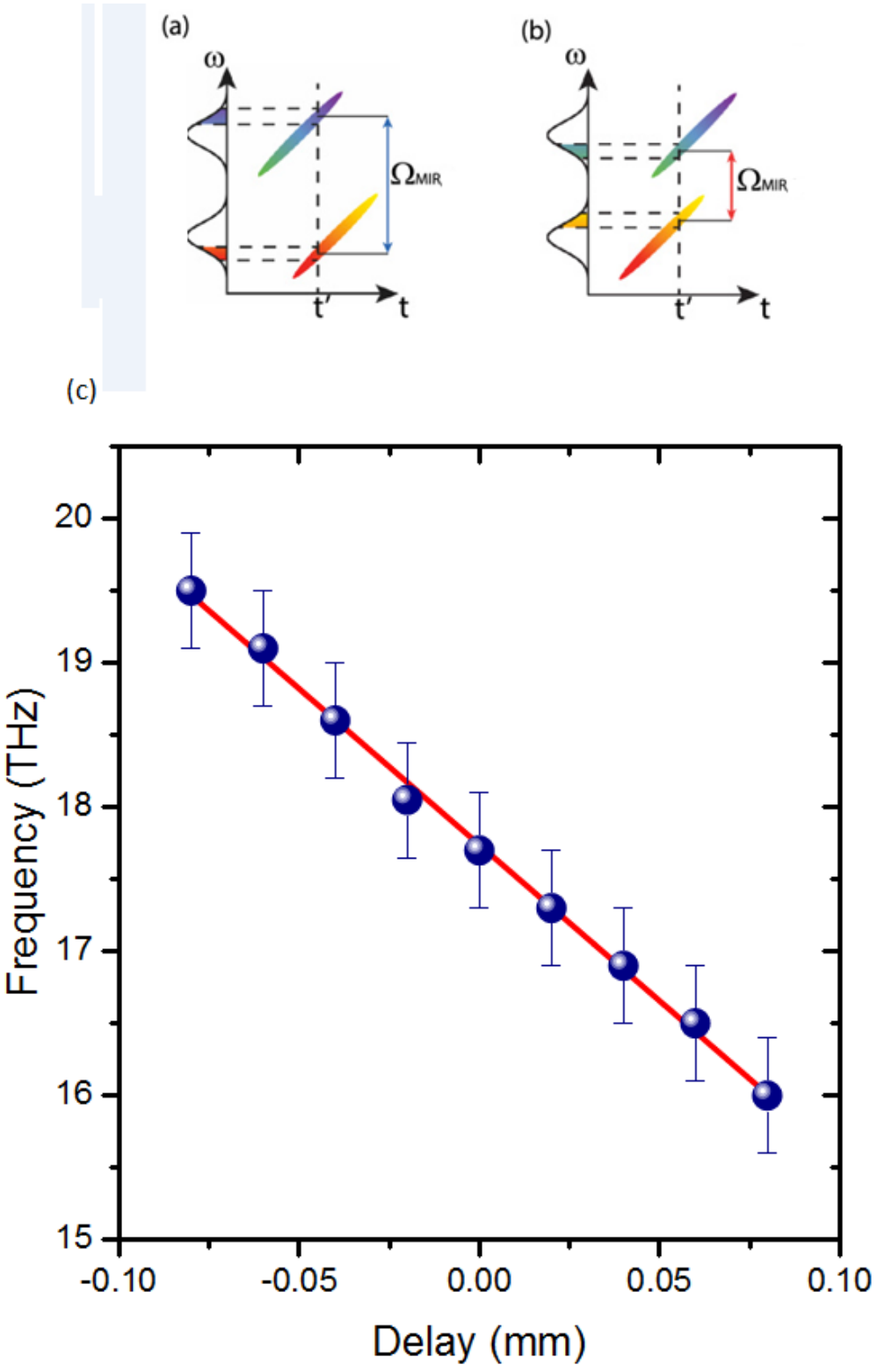

Figure 3.11: Frequency tunability of the DFG MIR. (a)-(b): when the time delay between the two NIR is shifted, the central frequency generated by DF is shifted as well. (c): experimental points together with the linear fit (red curve) and the error bars (0.8 THz that corresponds to the MIR bandwidth).

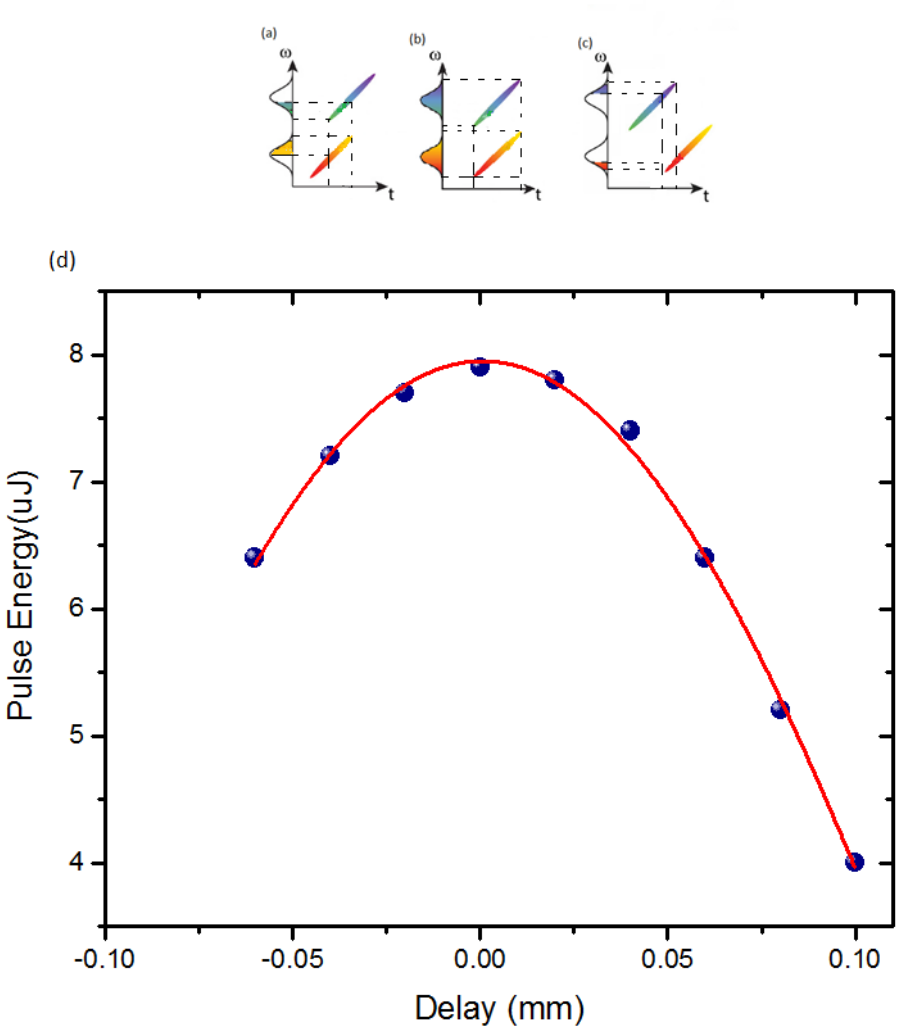

Figure 3.12: Energy variation of the DF generated MIR pulse as a function of the delay between the two NIR beams. (b): the time delay is zero [Figure 3.12 (b)], so all the frequency components of one NIR pulse interact with all the others of the second NIR pulse, hence resulting in a huge transfer of energy to the generated MIR beam. (a) and (c): when the time delay is negative or positive, the interaction is only between the lowest frequencies of one of the two NIR pulses and the highest frequencies of the others. (d): experimental data together with the gaussian fit (red line).

central MIR frequency by more than 1 or 2 THz we directly adjusted the OPA wavelengths, rather than varying the time delay between the two NIR beams.

Chapter 4

Light-induced superconductivity in YBCO

$YBa_2Cu_3O_{6+x}$ (YBCO) is a high temperature superconductor, whose critical temperature T_c monotonically increases with the hole doping level x, from 53 K (x = 0.50) to 93 K (x = 0.95). YBCO crystallizes in a centrosymmetric orthorhombic unit cell and comprises bilayers of CuO_2 planes, separated by an insuating layer containing Yttrium atoms and Cu-O chains, that control the hole doping x of the planes. The Cu-O chains serve as a charge reservoir for these planes: by increasing their oxygen content, one increases the hole doping of the CuO_2 planes. The $YBCO_{6.5}$ sample contains O-rich and O-deficient Cu-O chains (see Figure 1.1). The superconducting state is characterized by coherent tunneling of Cooper pairs both within bilayers and between them through the interbilayer region. Above Tc, interbilayer coupling is lost, while signatures of coherent tunnelling processes within the bilayers were found to persist up to temperatures far above Tc (as will be discussed in Section 4.3).

4.1 Phase diagram of underdoped YBCO

The underdoped compound $YBa_2Cu_3O_6$ is an antiferromagnetic insulator. Small hole-doping levels of 2% lead to a transition to a state that tends to be metallic, but still cannot be defined like that (we will discuss this state in the subsection dedicated to the *pseudogap*). This transition is accompained by the breaking of long-range antiferromagnetic order, which is replaced by a spin-glass phase that persists up to a temperature of 30 K. As the oxygen content is further increased, a superconducting phase develops with the highest transiton temperature of 93 K at optimal doping x =0.95.

Charge density wave order (CDW)

The superconducting phase shows a suppression at $1/8^{th}$ doping. At that doping level, x-ray scattering experiments revealed the presence of charge density wave (CDW) order [45]. The intensity of the diffraction peaks associated with the CDW rises with decreading temperature down to T_c; below T_c it starts to reduce with decreasing temperature. This behaviour suggested a competition between superconductivity and charge order. The formation of competing charge or spin order at $1/8^{th}$ doping is a general property of cuprates.

Light-induced superconductivity

Following resonant lattice excitation, signatures of light-induced superconductiong-like state have been found throughout the red region of the phase diagram of $YBa_2Cu_3O_{6+x}$. The first superconducting state induced by resonant lattice excitation was found in 2011 [47] in $La_{1.8-x}Eu_{0.2}Sr_xCuO_4$ at $1/8^{th}$ doping. In such material the superconducting phase is fully suppressed by a strong

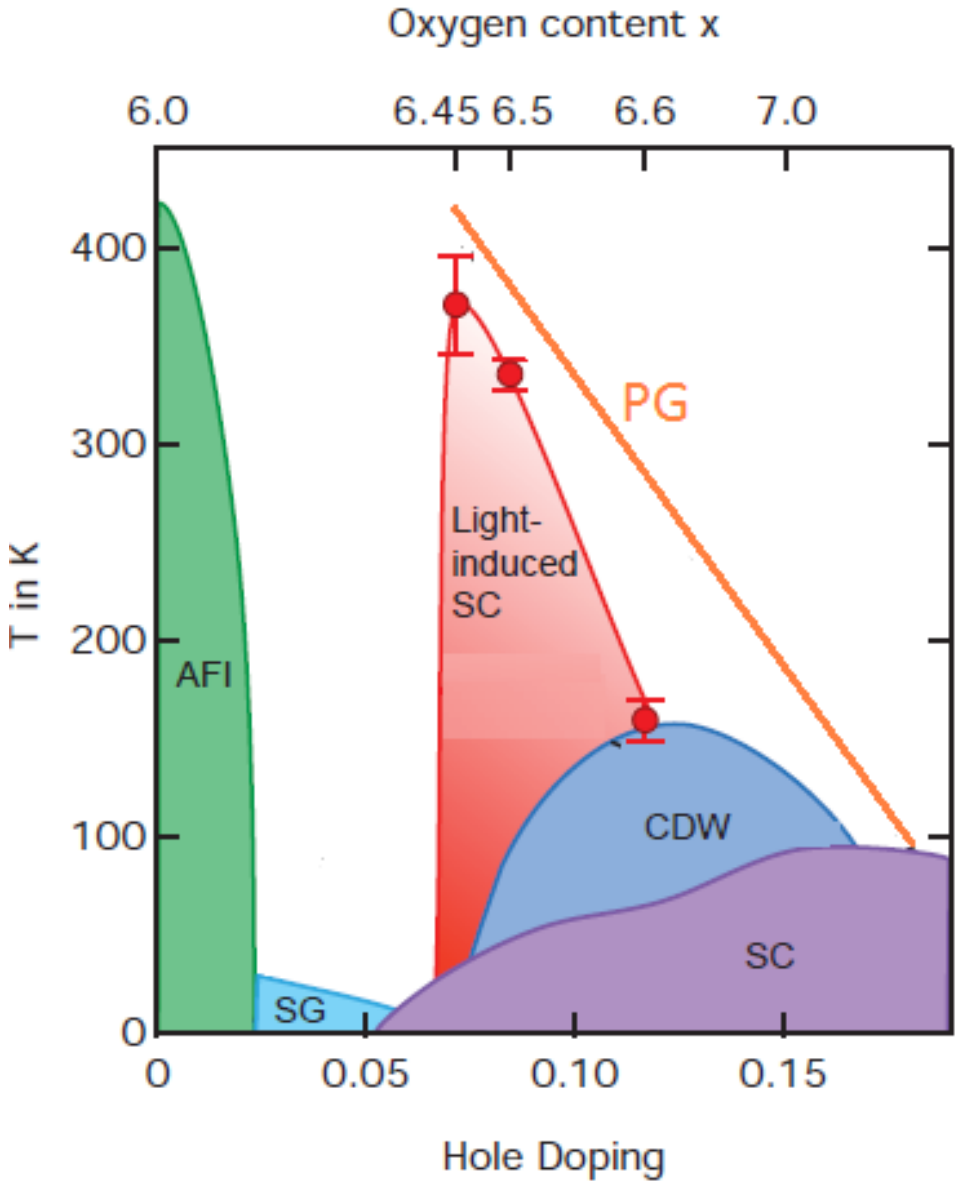

Figure 4.1: Hole-doping dependent phase diagram of $YBa_2Cu_3O_{6+x}$. The parent compound is an antiferromagnetic insulator. With increasing hole-doping, the long range antiferromagnetic order breaks down and the system tends to become metallic, with a spin glass (SG) phase at very low temperatures. The superconducting phase is suppressed at $1/8^{th}$ doping, at which charge density wave (CDW) order is observed. The pseudogap (PG) appear on the underdoped side of the phase diagram far above T_c. Following resonant lattice excitation, signatures of light-induced superconducting-like state have been found throughout the red region of the phase diagram.

ordering of the spins and charges in stripes. Resonant x-ray diffraction studies have shown that, after excitation of a proper phonon mode, the charge order melts at the same timescale as superconductivity appears; this suggests that the resonant lattice excitation restores the superconducting state by selectively melting the competing charge order [46]. The following discussion will continue later when we focus on light-induced superconductivity in $YBa_2Cu_3O_{6+x}$.

The pseudogap

It is worth spending a few words to describe a characteristic of the intermediate-doping (x = 0.85 $\rightarrow$ 0.90) and low-doping (x = 0.50 $\rightarrow$ 0.80) $YBa_2Cu_3O_{6+x}$ compounds: the presence of the *pseudogap*. In these materials, indeed, the conductivity along the c-axis shows a loss in low-frequency spectral weigh. Unlike the *real gap* that is present below T_c in these compounds, the pseudogap starts developing well above T_c (around room temperature), and transfer the spectral weigth - that is removed below 230 cm^{-1} - to high-frequency regions of the σ_1'spectrum, rather than to the delta function at zero frequency [35]. Furthermore, the spectral weight decreases linearly from room temperature down to the lowest measured temperature, *showing no anomalies at* T_c. The fact that the slope of the spectral weight curve is smooth through T_c, suggests that there is a close relationship between the superconducting gap and the pseudogap.

For the highly doped compound, there is no pseudogap. This can be understood by considering that in this compound, above T_c, the carrier transport is metallic both in the CuO_2 planes and normal to them. In the reduced doped compounds, in contrast, the transport is still metallic in the CuO_2 planes, whilst becomes nearly insulating normal to them. The pseu-

dogap is important because the light-induced superconducting state has been observed up to the temperature of the onset of the pseudogap.

Phonons in YBCO

By looking at th conductivity of $YBCO$, two components can be separated:a continuous background electronic conductivity that increases rapidly in magnitude as the doping level increases towards full doping, and a series of sharp phonon peaks. At high dopings, there are five strong phonons that manifest themselves in the c-axis optical conductivity σ_1; at room temperature, their frequencies are: 155, 194, 279, 312 and 570 cm^{-1}. At low dopings, many of these lines splits into two components. In particular, the higest-frequency mode, that is associated to the apical-oxigen vibration along the c-axis, splits into two components: a new phonon appears at 610 cm^{-1} in the nearly fully-doped material and moves to higher frequencies as the oxygen concentration is reduced, and becomes as high as 635 cm^{-1} in the x = 0.5 material. As can be seen from Figure 4.2, the low-frequency component increases in spectral weight as increasing doping: it is associated with the four-fold coordinated copper atom (the one that has both the two apical oxygen and the *chain oxygen* around). The high-frequency component is associated with the two-fold coordinated copper (that has only the apical oxygen around). Both of them imply the vibration along the c-axis of the apical oxygen atoms.

Let us briefly consider the modes different from the highest-frequency ones:

- the 155 cm^{-1} mode involves the motion of the *chain-copper and -oxygen* atoms, as well as of the apical-oxygen. This mode splits into two components as the doping level is decreased. From the analysis of these two components, can be deduced that the mode is driven by the chain

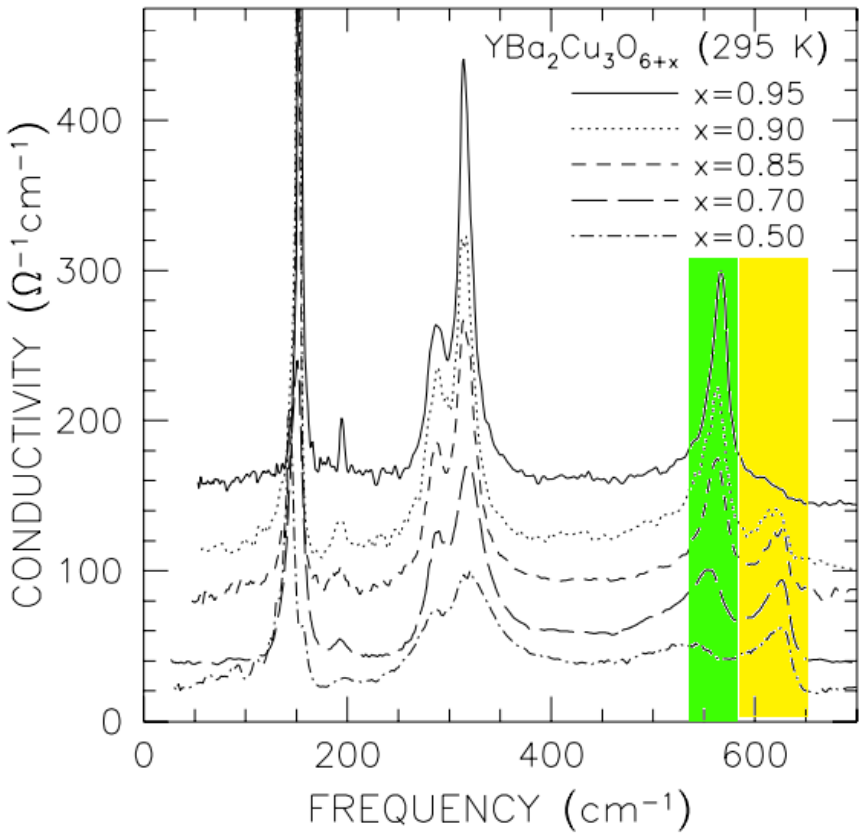

Figure 4.2: From [38]. The optical conductivity (σ_1) at 295 K fo $YBCO_{6+x}$ for radiation polarized alng the c-axis, for five oxygen dopings. In green the mode associated with the four-fold coordinated copper atom. In yellow, the mode associated with the two-fold coordinated copper.

atoms rather than by the apical-oxygen;

- the 194 $cm{-}1$ mode has low spectral weight that decreases with decreasing doping level; at x = 0.50 it is disappeared;

- the 279 $cm{-}1$ mode consists in a *chain-oxygen* vibration, polarized in the c-direction;

- the 315 $cm{-}1$ mode is a plane-bending vibration of oxygen atoms in the CuO_2 planes.

4.2 Probing superconductivity: signatures of Josephson coupling

Superconductors at equilibrium exhibit two characteristic physical properties: zero d.c. resistance and expulsion of static magnetic field. We are interested in controlling the lattice dynamics with light, in order to transiently induce a superconducting state above the equilibrium critical temperature of the material. Since the light-induced state lasts for at most some picoseconds, measuring electrically its d.c. resistivity or verifying that the material under investigation is expelling a static magnetic field it is impossible. However, there are experimental techniques useful to retrieve the transient optical properties of a material (how this is done is explained in Section 5.1); from these optical properties one can draw conclusions on the nature of the transient state. Here, we try to summarize which are the signatures of the presence of a Josephson coupling between two superconducting layers separated by an insulating region, that are easily recognizable from the transient optical properties. In fact, it has been demonstrated that the

layered structure of high-T_c cuprates, like $YBCO$, can be modelled - in the superconducting state - by a stack of Josephson junctions [41].

The *charge-density modes* or *plasma modes* of a classical compressible charged fluid correspond to the condition that an arbitrarily weak density fluctuation with wave-vector k and frequency ω generate a finite electromagnetic response [39]. Such a response is described by the imaginary part of the inverse of the longitudinal dielectric function, $\mathrm{Im}\left\{\frac{1}{\epsilon_L(\omega,k)}\right\}$. So ,plasma modes correspond to poles of this function or, equivalently, to zeros of the longitudinal dielectric function, $\epsilon_L(\omega,k)=0$. In the relevant limit for spectroscopy, k$\rightarrow$0, there is no need to distinguish between ϵ_L and the transverse response, ϵ_T, since they coincide: from now on we simply refer to ϵ. It can be that the dissipation *in the normal state* is large enough to cause an *over-damped* charge response, preventing in this way the appearance of any charge-density collective response. On the other hand, the condensate of a *superconductor* is characterized by the absence of dissipation at least for frequencies much smaller than the superconducting gap, implying that $\epsilon(\omega,k)=0$ must occur at some finite frequency. Hence, in materials where the dissipation in the normal state is large enough to cause an over-damped charge response, the charge-density collective mode must emerge at some finite frequency within the frequency window of dissipationless flow, when the material becomes superconducting. In contrast, if the plasma mode is not over-damped in the normal state, the transition into the superconducting state affects the plasma frequency only marginally. This behaviour is observed for c-axis optical response of the cuprate superconductors.

Another signature of the existence of a Josephson coupling between the CuO_2 layers in a cuprate superconductor is an edge in the reflectivity, that appears at the same frequency such that $\epsilon(\omega,k)=0$ [41].

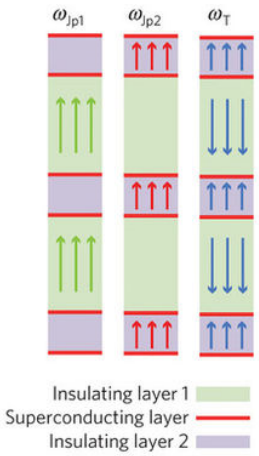

Figure 4.3: Representation of the longitudinal modes (ω_{J_p1}, ω_{J_p2}) and of the transverse mode (ω_T in a bilayer cuprate that in the superconducting state is viewed as a stack of Josephson junctions. Arrows indicate the direction of the current [41].

One of the most significant parameters that characterize the Josephson coupling between two neighbouring superconducting planes is the *Josephson coupling* energy term, J. It is proportional to the *critical current* due to the flow of electrons between the layers and to the superconducting density along the the c-axis, ρ_c, as well as - in a single Josephson junction -to the square of the Josephson plasma frequency, ω_{J_p}. In the London picture [40], its value is proportional to the limit of $\omega\,\mathrm{Im}\{\sigma(\omega)\}$ for $\omega \to 0$. Putting all together:

$$J \propto \frac{1}{d}\rho_c \propto \omega_{J_p}^2 \propto \omega\,\mathrm{Im}\{\sigma(\omega)\}|_{\omega\to 0} \tag{4.1}$$

where d is the thickness of the single Josephson junction.

In a bilayer material like $YBCO$, one expects to find - in the superconducting state - two longitudinal plasma modes at ω_{J_p1} and ω_{J_p2}, that correspond to a supercurrent in the interbilayer and intrabilayer region and manifest themselves as peaks in the loss function, $-\,\mathrm{Im}\left\{\frac{1}{\epsilon_L(\omega,k\to 0)}\right\}$, and edges

in the reflectivity, and one transverse plasma mode at ω_T that corresponds to the out-of-phase oscillations of the interplane currents within and between pairs of layers and manifest itself as a peak in the c-axis optical conductivity $\sigma_1(\omega)$ (see Figure 4.3). In this case the Josephson coupling value is $J \propto \frac{\omega_{J_{p1}}^2 \omega_{J_{p2}}^2}{\omega_T^2}$.

To conclude this section, dedicated to the description of the signatures on the optical properties of a superconducting state, it is worth recalling that the Drude-Lorentz model of charge conduction gives as result: $\sigma_2 \propto \frac{1}{\omega}$, as well as a zero-frequency delta function in the real part of the optical conductivity, in the limit of *zero dissipation*. So, we expect to find something like this in the imaginary part of the conductivity along the c-axis, when the bilayer cuprate $YBCO$ becomes superconducting.

4.3 Inducing SC with light in YBCO

Here we briefly report on the results obtained by *Hu et al.*, by pumping the $YBa_2Cu_3O_{6.5}$ bilayer cuprate with 300 fs pulses, polarized along the c-axis of the sample, tuned to 670 cm^{-1} frequency, with a relative bandwidth $\Delta\nu/\nu_0$ of 30%, and a maximum fluence of 4 $mJcm^{-2}$, that corresponds to peak electric fields of 3 MV/cm.

Before that, we show in Figure 4.4 the equilibrium c-axis optical properties of the sample, below T_c. Superconductivity is evidenced by the $1/\omega$ divergence in the imaginary part of the optical conductivity. Two longitudinal Josephson plasma modes appears as two peaks in the loss function, $-\,\mathrm{Im}\{1/\epsilon\}$, and two edges in reflectivity ($\approx$ 30 cm^{-1}, $\approx$ 475 cm^{-1}). The transverse plasma mode appears as a broad peak around 400 $cm{-}1$ in the real part of the optical conductivity.

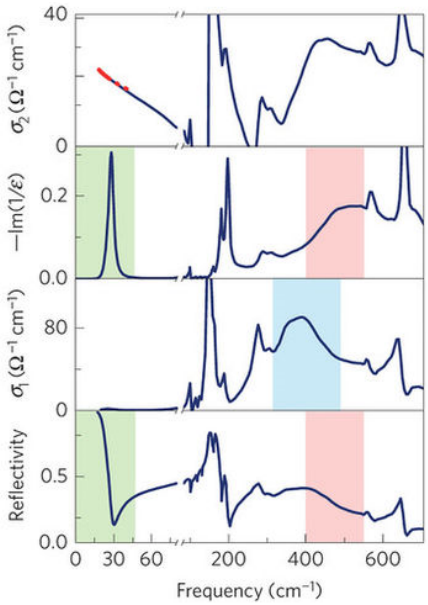

Figure 4.4: From [34]. Equilibrium c-axis optical properties for $YBa_3Cu_3O_{6.5}$, below T_c. Superconductivity is evidenced by the $1/\omega$ divergence (red dashed-dotted line) in the imaginary part of the optical conductivity. Two longitudinal Josephson plasma modes appears as two peaks in the loss function, $-\,\mathrm{Im}\{1/\epsilon\}$, and two edges in reflectivity ($\approx 30\ cm^{-1}$, $\approx 475\ cm^{-1}$ shaded areas). The transverse plasma mode appears as a broad peak around 400 $cm{-}1$ in the real part of the optical conductivity (blue shaded area).

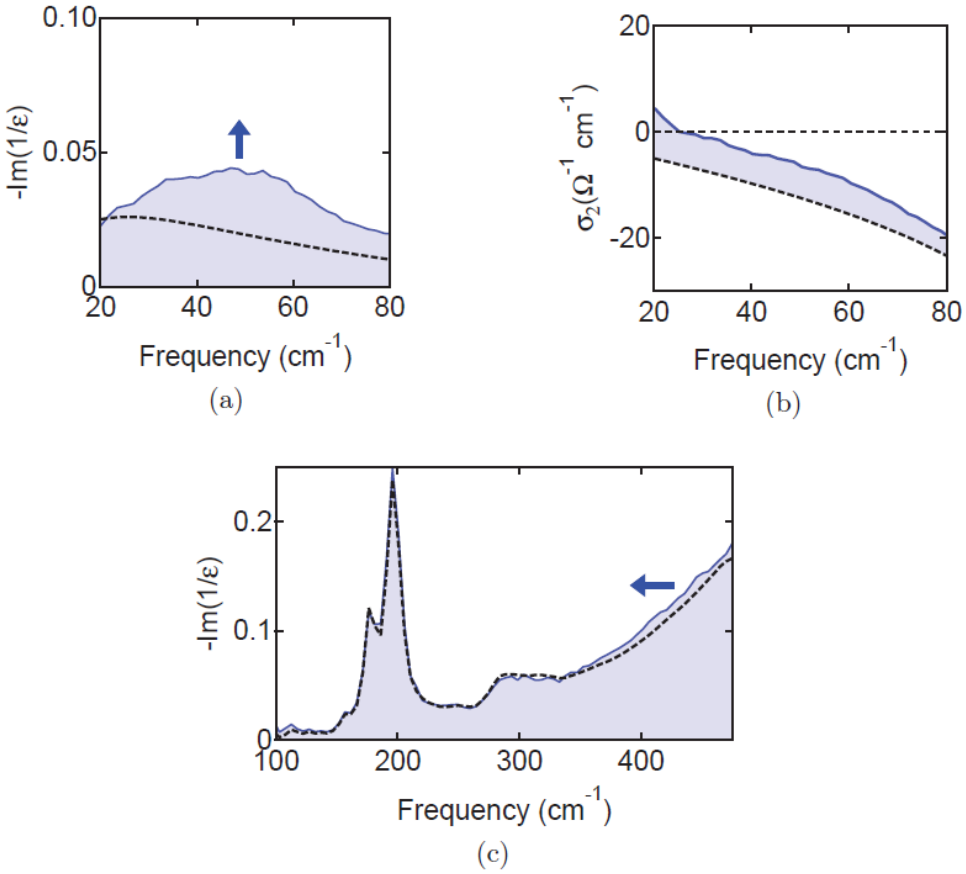

Figure 4.5: Equilibrium (dashed black line) and transient (blue line) optical properties of $YBa_2Cu_3O_{6.5}$ $\approx$ 0.5 ps after resonant lattice excitation above Tc. (a) A peak in the loss function appears at 50 cm^{-1}, which can be attributed to the interbilayer plasma resonance. (b) The slope of σ_2 increases towards low frequencies. (c) The loss function peak of the intrabilayer junction shifts to lower frequencies. Images adapted from [34].

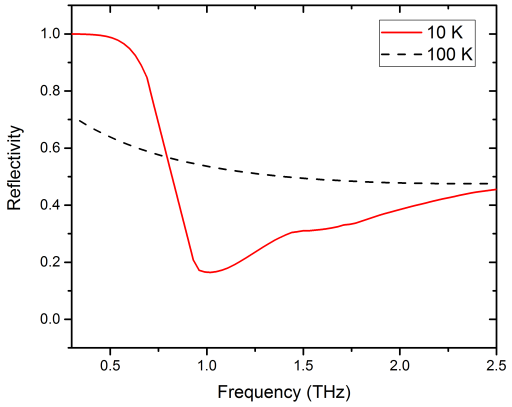

Figure 4.6: Equilibrium reflectivity of $YBCO_{6.5}$. The JPR, that can be seen at 10 K as an edge in reflectivity around 1 THz, disappears above T_c, at 100 K.

The optical properties, acquired above T_c, 0.5 ps after the excitation show that (see Figure 4.5): a peak in the loss function appears at 50 cm^{-1}, which can be attributed to the emergence of the interbilayer longitudinal plasma mode, that is not present at equilibrium above T_c (see Figure 4.6);σ_2 increases towards low frequencies, assuming at a certain point positive values, whilst at equilibrium always lies below zero; the loss function peak of the intrabilayer junction shifts to lower frequencies, with respect to the undriven case.

An interpretation of the data based on *transient superconducting coherence induced above* T_c is the most plausible. In fact, the photoinduced peak in the low-frequency loss function is very close to the equilibrium ω_{J_p1}; this suggests that the light-induced transport above T_c involves a density of charge carriers that behaves in the same way as the density of Cooper pairs that tunnell between planes in the equilibrium superconductor. Furthermore, the photoinduced change in the imaginary conductivity $\Delta\sigma_2(\omega, 0.5ps)$ above T_c, defined as $\sigma_2(\omega, 0.5ps) - \sigma_2(\omega, equilibrium)$ tracks very well $\sigma_2(\omega, equilibrium, T < T_c) - \sigma_2(\omega, equilibrium, T > T_c)$.

It has been pointed out that the *total coherent spectral weight* associated with the two longitudinal plasma modes - that scales with $\omega^2_{J_p1} + \omega^2_{J_p2}$ I [35] - after the excitation, assumes the same value it had at equilibrium (in fact the value of ω_{J_p2} redshifts, while the low-frequency mode appear at ω_{J_p1}). This means that the formation of the low-frequency interbilayer coupling (appearance of the low-frequency longitudinal plasma mode) occurred at the expense of the interbilayer coupling (ω_{J_p2} redshifts), that is still present above T_c at equilibrium, and it is reduced immediately after the excitation. This suggests that light only rearranges the relative tunnelling strengths of the two Josephson junction in the unit cell of $YBa_2Cu_3O_{6.5}$, with coherence being transferred from the intrabilayer to the interbilayer region.

4.4 Non-equilibrium control of complex solids by nonlinear phononics

The response of a crystal lattice to a resonant excitation of an infrared-active phonon mode, by means of optical fields at strengths in excess of $100kV/cm$, can be described by separating the crystal Hamiltonian into its linear and nonlinear terms: $H = H_{lin} + H_{NL}$. The linear response is described by the potential energy term $V_{lin} = \frac{1}{2}\omega^2_{IR}Q^2_{IR}$, where Q_{IR} is the normal coordinate of the IR phonon-mode and ω_{IR} its eigenfrequency.

In the limit of lowest order (cubic) coupling of the IR-active mode to other modes with generic coordinate Q_R, the lattice potential describing the nonlinear interaction is written as

$$V_{NL} = \frac{1}{2}\omega^2_R Q^2_R - a_{12}Q_{IR}Q^2_R - a_{21}Q^2_{IR}Q_R \tag{4.2}$$

where a_{ij} are anharmonic coupling coefficients. For a centrosymmetric crystal (like $YBa_2Cu_3O_{6.5}$), the term $a_{12}Q_{IR}Q_R^2$ is zero because the IR-active modes are odd in symmetry whereas Q_R^2 is even, so that their product vanishes. The term $a_{21}Q_{IR}^2Q_R$ is nonzero only if Q_R is even in symmetry, i.e. if it is a Raman-active mode. So, equation 4.2 can be restated as

$$V_R = \frac{1}{2}\omega_R^2 Q_R^2 - a_{21}Q_{IR}^2 Q_R \tag{4.3}$$

From this equation, it is evident that, for a given distortion $\bar{Q}_{IR}$ of the infrared-active mode, the nonlinear phonon interaction induces a displacement from the origin of the vertex of the parabola of the Raman mode's energy potential V_R - expressed as a function of the Raman coordinate Q_R. The abscissa of the minimum is proportional to Q_{IR}^2. This means that, as soon as Q_{IR} oscillates around zero, the Raman-active mode undergoes a displacement that has a fixed direction.

For pulsed excitation of the infrared-active mode Q_{IR}, the coupled dynamics are described by the equations of motion:

$$\begin{cases} \ddot{Q}_{IR} + 2\gamma_{IR}\dot{Q}_{IR} + \omega_{IR}^2 Q_{IR} = f(t) + 2a_{21}Q_{IR}Q_R \\ \ddot{Q}_R + 2\gamma_R\dot{Q}_R + \omega_R^2 Q_R = a_{21}Q_{IR}^2 \end{cases} \tag{4.4}$$

where γ_i is the damping constant of mode i and $f(t)$ is the driving field resonant with the IR-active mode, and is written as $f(t) = E_0 F(t)\sin(\omega_{IR}t)$. E_0 is the peak amplitude of the electric field, and $F(t)$ is a normalized Gaussian envelope function. We see here what we have already predicted in the discussion on the shifting of the vertex of the parabola $V_R(Q_R)$: the force $a_{21}Q_{IR}^2$ that drives the anharmonically coupled Raman-active mode has a fixed direction, that is independent on the sign of Q_{IR}. Hence, the atoms of

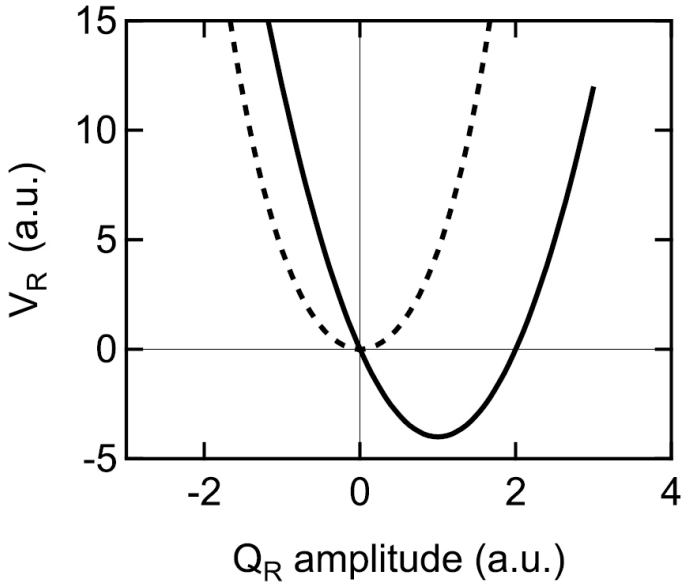

Figure 4.7: For a static displacement $\bar{Q}_{IR}$ of the infrared-active mode, the nonlinear phonon interaction induces a shift of the parabola of the Raman mode's energy potential V_R - expressed as a function of the Raman coordinate Q_R - from the origin. The new V_R has now the minimum for a value $\bar{Q}_R$ that is different from zero.

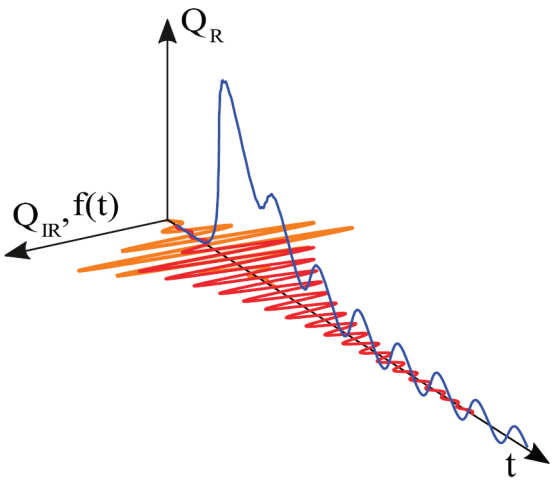

Figure 4.8: From [36]. The dynamical response of two coupled modes within cubic coupling. Following excitation by the electric field$f(t)$ (orange), the infrared-active mode Q_{IR} (red) starts to oscillate coherently about the equilibrium position, while Q_R (blue) undergoes a directional displacement, which scales with Q_{IR}^2

.

the crystal, oscillate along the infrared coordinate Q_{IR} and are simultaneously are displaced along the Raman coordinate Q_R (see Figure 4.8). If the optical excitation is short compared to the period of the Raman mode, Q_R exhibits coherent oscillations around the displacement amplitude.

4.5 Enhancing superconductivity by nonlinear phononics in YBCO

In this section, we report on the appication of nonlinear phononics to the specific case of $YBa_2Cu_3O_{6.5}$. In experiments [42, 43, 44], was shown that in all the YBCO compounds investigated - YBCO- 6.6, 6.8, and 7 - the transition temperature increased with the application of pressure, that was found to cause a reduction in the distance between the planar copper atoms

and the apical oxygen atoms in the interbilayer region. While this effect was very small for optimally doped $YBCO_7$ samples, it increased rapidly with decreasing hole doping levels. Based on these results, the increase in transition temperature was proposed to be due to a charge redistribution from CuO_2 planes to interbilayers $Cu-O$ chains, effectively increasing the hole doping of the planes.

These results raised the question of whether the modulation of this $Cu-O$ distance by resonant excitation of the vibrational mode of the apical oxygen could enhance superconductivity and increase the transition temperature above its equilibrium value. In Section 4.3, we saw that the answer is "yes". *Mankowsky et al.* went a step further [37] : they pumped the $YBa_2Cu_3O_{6.5}$ crystal above T_c with pump pulses made resonant with the mode associated with oscillations of the apical oxygen in the Cu-O chains and monitored the lattice time evolution by means of time-resolved x-ray diffraction. The transient lattice structure revealed a decrease in the distance between the apical oxygen and Cu atoms in the superconducting planes. The Cu atoms are simultaneously driven away from one another within the bilayers and towards one another between different bilayers. This behaviour is intuitively consistent with the broadband THz probe measurements, which indicated that the appearance of interlayer coupling comes above T_c in the driven state at the expenses of intrabilayer coupling strength. The displacement is approximately 0.63% of the equilibrium intra-bilayer distance. The transient crystal structure was reconstructed and is shown in Figure 4.9.

Furthermore, x-rays data revealed a decay of the atom positions to the equilibrium lattice configuration on the same timescale as the relaxation of induced coherent interlayer transport measured in the time-domain THz-spectroscopy experiment [34]. This suggests an intimate connection between

the distance of the CuO_2 planes and the coherent tunnelling of the supercurrent in the c-axis direction. The pump pulses in the x-ray experiment had the same characteristics - in terms of duration, maximum fluence, peak electric field, relative bandwidth, as well as central frequency - as the ones in the above mentioned pump-probe experiment [34], so the comparison of the excited state times toward equilibrium in the two cases was meaningful.

The experiment represented also a further confirmation that nonlinear phononics, together with density functional theory (DFT), can be used as a tool for the dynamical control of the lattice structure: DFT calculations predicted that the pumped IR mode coupled strongly with four Raman modes, all of them involving a distortion of the apical oxygen toward the CuO_2 planes; the theory of nonlinear phononics in turn that the lattice is distorted along the linear combination of the atomic motions associated with the Raman modes that effectively couples to the driven IR mode. This is what was observed.

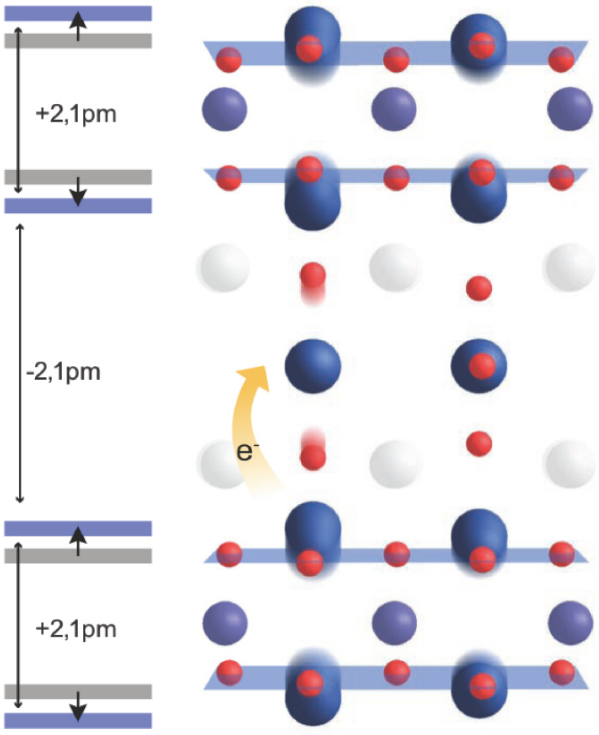

Figure 4.9: From [37]. Sketch of the reconstructed transient crystal structure of $YBaCuO_{6.5}$. The atomic displacements from the equilibrium structure involve a decrease in interbilayer distance, accompained by an in increase in intrabilayer distance

.

Chapter 5

Controlling LIS using narrowband excitation

5.1 Time-resolved THz spectroscopy

To see how the material evolves after the (light) excitation, one has to look at its optical properties. They can be retrieved by means of time-resolved pump-probe THz spectroscopy: the response of the material is monitored on a subpicosecond time scale by measuring the reflection changes of a delayed 'probe' pulse at THz frequencies, induced by the MIR pump pulse. In the THz frequency regime indeed can be found the fingerprints of the superconducting light-induced state. In the following we show the experimental setup of our pump-probe experiment (see Figure 5.1) and how to retrieve the transient optical properties of the material starting from the measured electro-optic traces.

The MIR *pump* - linearly polarized along the c-axis of the crystal - was sent to the sample at normal incidence. The c-axis linearly polarized THz*probe*, generated through OR in ZnTe nonlinear crystal and covering

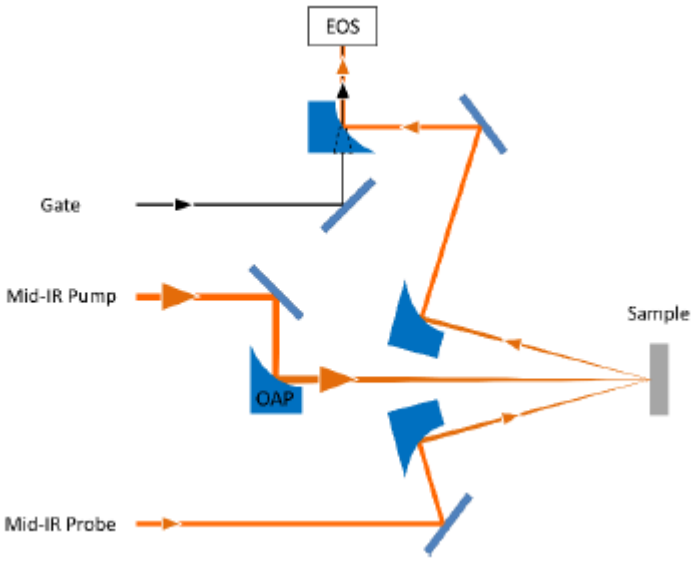

Figure 5.1: Schematic of the pump-probe setup. OAP: off-axis parabolic mirrors.

a bandwidth from 20 to 85 cm-1 (see Figure 2.9 in Section 2.4.1), hit the sample with an angle of 30° with respect to the normal to the sample and is, after the reflection from the sample, electro-optically sampled in another ZnTe crystal by a low-energy *gate* pulse at 800 nm, coming directly from the laser. See Figure 5.1.

A pump-probe experiment in general starts with the acquisition of the static electro-optic sampling of the probe pulse: the probe is scanned by the gate pulse by varying the time delay t between the two beams (the pump pulse being off). Figure 5.3 shows a typical time trace acquired in this way. Then, t is fixed such that the gate always samples the same point of the probe (we usually "sit on the peak of the probe"), while the time delay τ between the pump and the probe varies from negative to positive values (1D trace). In this way, the pump-induced change in the peak amplitude value of the reflected probe pulse is measured at each time delay τ during the

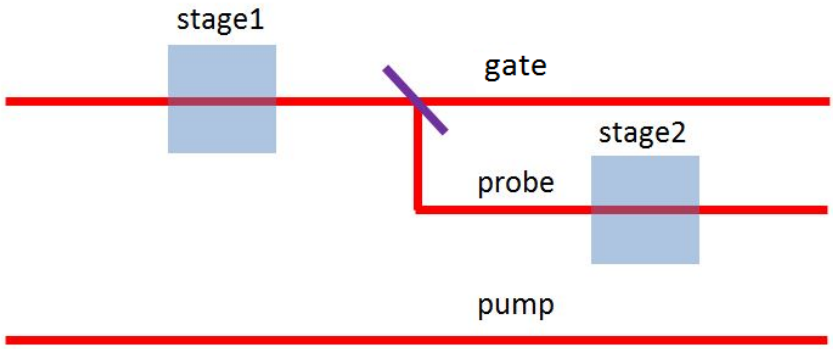

Figure 5.2: Schematic of the delay stages for pump-probe measurements. By moving only the stage 2, the 1D pump probe trace is obtained. By moving the stage 2, the 2D scan of the probe is obtained.

dynamically evolving response of the material. See Figure 5.4.

Analysing the 1D trace, one can select different values of the pump-probe delay τ. For each of this , one can acquire the respective 2D trace: once τ is fixed - i.e. the relative delay between excitation and sampling is fixed - the THz pulse is scanned by changing the internal delay t with respect to the gate. In this way, each point of the THz time trace probes the response of the material at the same instant of time after the excitation. In Figure 5.2 is explained how 1D and 2D traces were performed in practice.

For a given pump-probe delay τ, both the equilibrium reflected probe pulse $E_R^{unpumped}(t)$ and the pump-induced change $\Delta E_R(t)$, i.e. $E_R^{pumped}(t) - E_R^{unpumped}(t)$ were measured simultaneously (see Figure 5.5). This was achieved by chopping both the pump and the probe beams, and measuring the reflected electric field with two lock-in amplifiers, one connected to the pump's chopper and the other to the probe's chopper. The frequency resolved data $\tilde{E}_{unpumped}(\omega, \tau)$ and $\Delta\tilde{E}_R(\omega, \tau)$, for a given τ, can be reconstructed by Fourier transforming the measured traces along the EOS coordinate t.

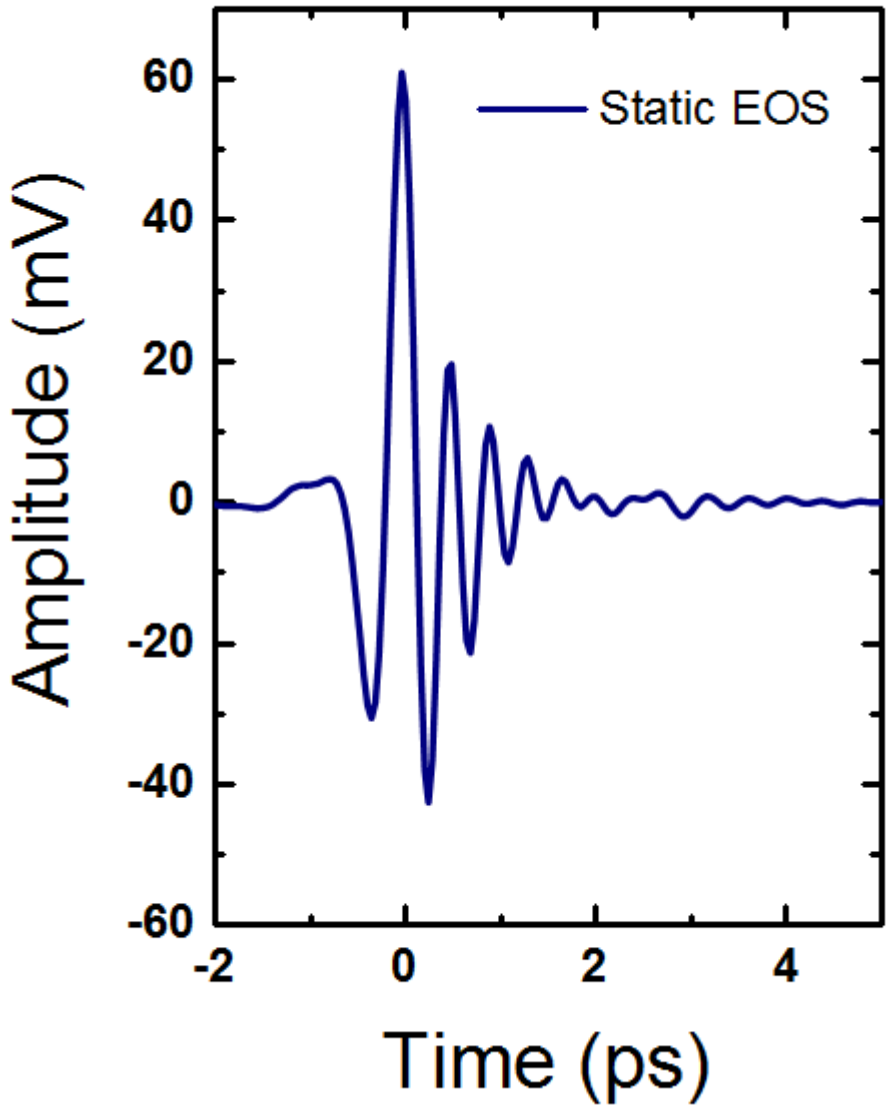

Figure 5.3: EOS static trace of the THz probe at 100K.

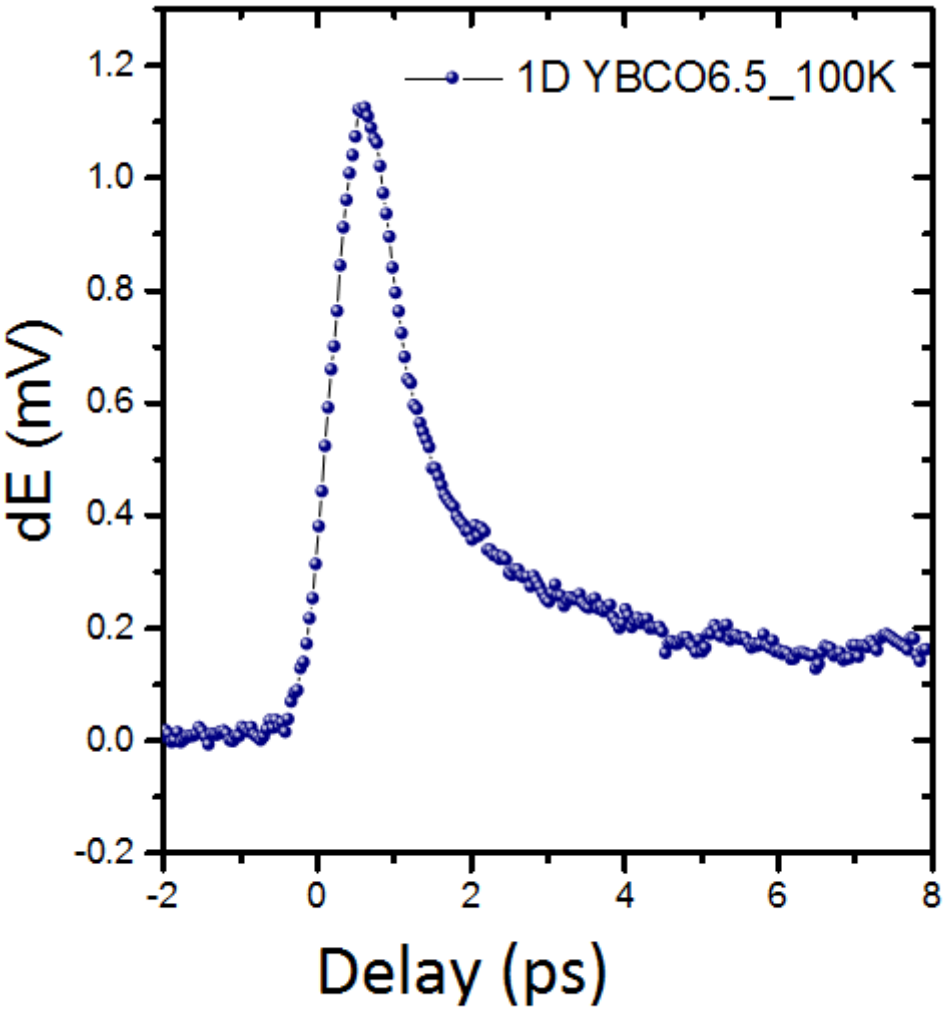

Figure 5.4: $\Delta E_R(\tau)$, defined as $E_R^{pumped}(\tau) - E_R^{unpumped}(\tau)$. This value represents the pump-induced change in the peak amplitude value of the reflected probe pulse as a function of the time delay τ between the pump and the probe pulses during the dynamically evolving response of the material (1D trace). The data are taken on $YBCO_{6.5}$ at 100K. The pump-central frequency is resonant with the phonon mode at 19.28 THz.

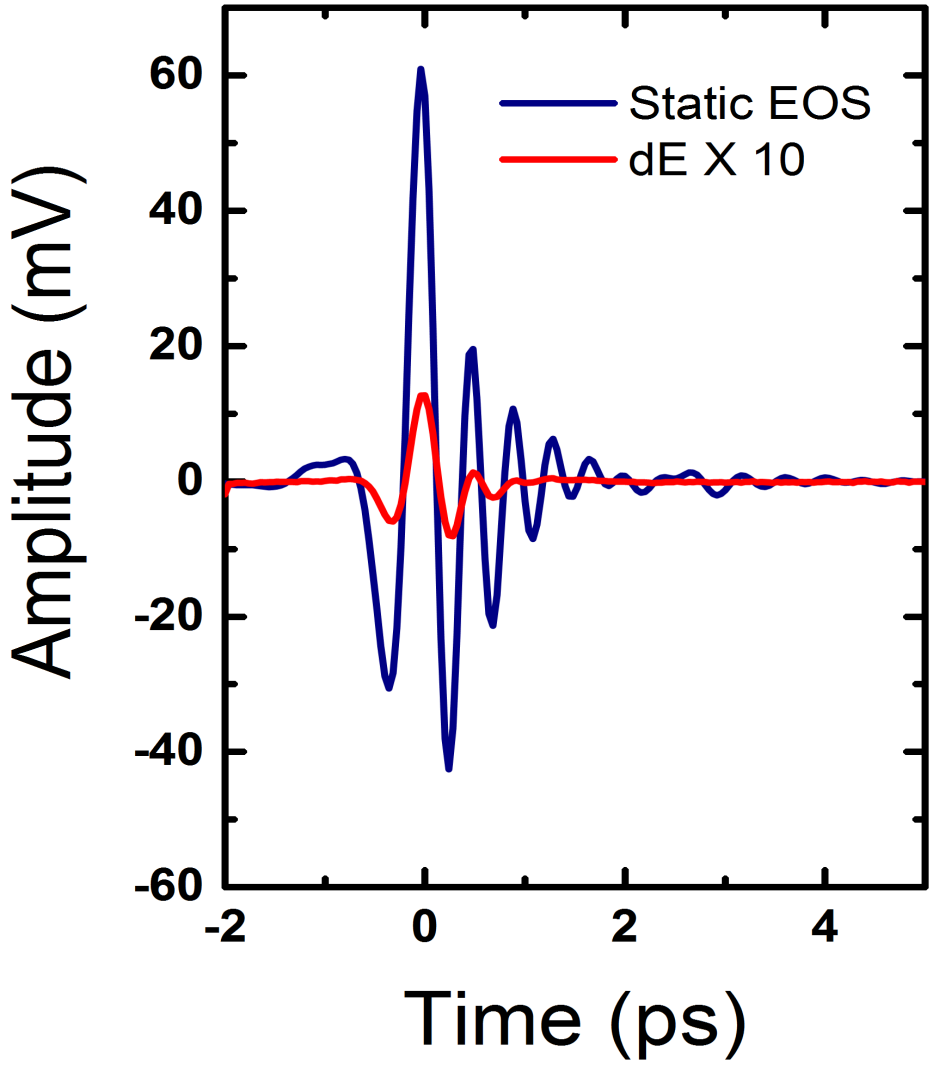

Figure 5.5: Static EOS trace of the probe together with $\Delta E_R(t)$, defined as $E_R^{pumped}(t) - E_R^{unpumped}(t)$. t is the internal time delay between the probe and the gate. The pump-probe time delay τ value is the one at the peak of the curve in figure 5.4. Data are taken at 100 K. The pump-central frequency is resonant with the phonon mode at 19.28 THz.

.

The complex reflection coefficient of the photo-excited sample, $\tilde{r}'(\omega,\tau)$, was determined from the normalized pump-induced changes to the electric field $\Delta\tilde{E}_R(\omega,\tau)/\tilde{E}_R(\omega,\tau)$:

$$\frac{\Delta\tilde{E}_R(\omega,\tau)}{\tilde{E}_R(\omega,\tau)} = \frac{\tilde{r}'(\omega,\tau)-\tilde{r}(\omega)}{\tilde{r}(\omega)} \tag{5.1}$$

where the stationary reflection coefficient $\tilde{r}(\omega)$ was evaluated from the equilibrium optical properties ([35]). From $\tilde{r}'(\omega,\tau)$, the change in reflectivity, $\frac{\Delta R}{R}(\omega,\tau)$, that is $(|\tilde{r'}(\omega,\tau)|^2-|\tilde{r}(\omega,\tau)|^2)/|\tilde{r}(\omega,\tau)|^2$ was extracted, for a given pump-probe delay τ.

Formula 5.1 directly gives us all the material parameters we need. Here we show how the knowledge of the amplitude and the phase of the static and transient probe's reflectivity, allows for extracting the real and imaginary parts of time- and frequency- dependent optical conductivity $\sigma_1(\omega,\tau)+i\sigma_2(\omega,\tau)$. For normal incidence, the complex reflection coefficient r - associated to an electromagnetic wave that comes from medium "zero" and is reflected by medium "one" - is given by $\tilde{r}=\frac{\tilde{N}_0-\tilde{N}_1}{\tilde{N}_0+\tilde{N}_1}$. $\tilde{N}_i$ is the complex refraction index of the medium "i"($\tilde{N}=n+ik$ where n is the real refractive index and k is the extinction coefficient. $\tilde{N}=\sqrt{\tilde{\epsilon}\mu}$). In our case the beam comes from the air so $\tilde{N}_0$=1. From $\tilde{r'}$, by applying the formula $\tilde{r'}=\frac{1-\tilde{N}'_1}{1+\tilde{N}'_1}$, one can extract both n' and k' ($\tilde{N}'=n'+ik'$) for the excited state, at any given instant of time τ after the excitation. In this way one is able to track the time-evolution of the excited material. In fact, from n' and k' it is possible to calculate all the optical constants:

$$\begin{aligned} \sigma_1 &= \frac{\epsilon_0}{4\pi} 2nk\omega \\ \sigma_2 &= \frac{\epsilon_0}{4\pi}(1+k^2-n^2)\omega \\ \epsilon_1 &= n^2 - k^2 \\ \epsilon_2 &= 2nk \\ \mathrm{Im}\left\{-\frac{1}{\epsilon}\right\} &= \frac{2kn}{4k^2n^2 + (n^2-k^2)^2} \end{aligned} \tag{5.2}$$

Notice that in our case the probe hits the sample with an angle of 30°, so that the Fresnel formula for normal incidence has to be substituted with the proper one; anyway, the way of proceeding to extract the optical constants of the material is the same. All the results that we presented here hold in the *bulk model*, that assumes that the pump penetration depth is equal to the probe penetration depth. But, actually, this is not the case.

The mismatch between the several-μm penetration depth of the THz probe and the few-hundreds nm one of the 15-μm pump pulse has to be taken into account. Then, since the probe interrogates a volume that is between 10 and 20 times larger than the pump-transformed region beneath the surface, one can assume that the sample is photoexcited *homogeneously* within a thickness corresponding to the pump penetration-depth d_{pump}. See figure 5.6. This is called *single-layer* or *thin-film* model. The penetration depth d_{pump} is given by $d = \frac{c}{4\pi\nu_0 k(\nu_0)}$, where k is the extinction coefficient of the sample in the normal state, and ν_0 is the central frequency of the pump.

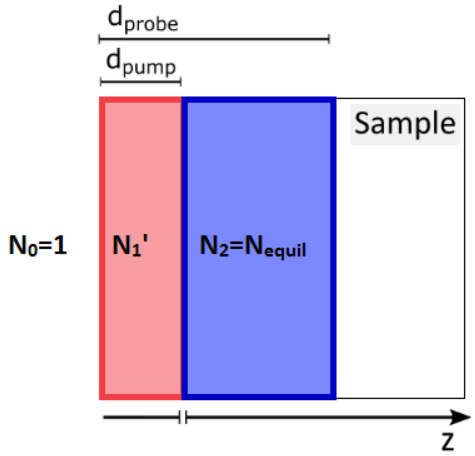

Figure 5.6: Difference in the penetration depths of the pump and the probe. Schematic representation of the *single-layer* or *thin-film* model.

We consider the following system of equations:

$$\begin{cases} \tilde{r'} = \tilde{r_{01}} - \dfrac{1}{\tilde{r_{01}}}\dfrac{N_1'}{N_0}t_{01}^2\left(\dfrac{1}{1+\tilde{r_{01}}\tilde{r_{12}}\exp(2i\delta)} - 1\right), with N_0 = 1 \\ \delta = 2\pi d\dfrac{N_1'}{\lambda} \\ \tilde{r_{01}} = \dfrac{N_0 - N_1'}{N_0 + N_1'}, with N_0 = 1 \\ \tilde{r_{12}} = \dfrac{N_1' - N_2}{N_2 + N_1'}, with N_2 = N_{equil} \\ t_{01} = \dfrac{2N_0}{N_0 + N_1'}, with N_0 = 0 \end{cases} \tag{5.3}$$

where: N_0=1 because we are assuming that the probe pulse comes from the vacuum; $\tilde{r_{01}}$ is the complex reflection coefficient at the interface between vacuum and the photo-excited layer, and t_{01} is the respective complex transmission coefficient; $\tilde{r_{12}}$ is the complex reflection coefficient at the interface between the photo-excited layer and the region accessible only to the probe; we assume that such region is not perturbed by the probe, this is why we impose $N_2 = N_{equil}$, where N_{equil} is taken from literature; λ is the wavelength of the probe pulse; indeed we are considering the reflection of the probe pulse:

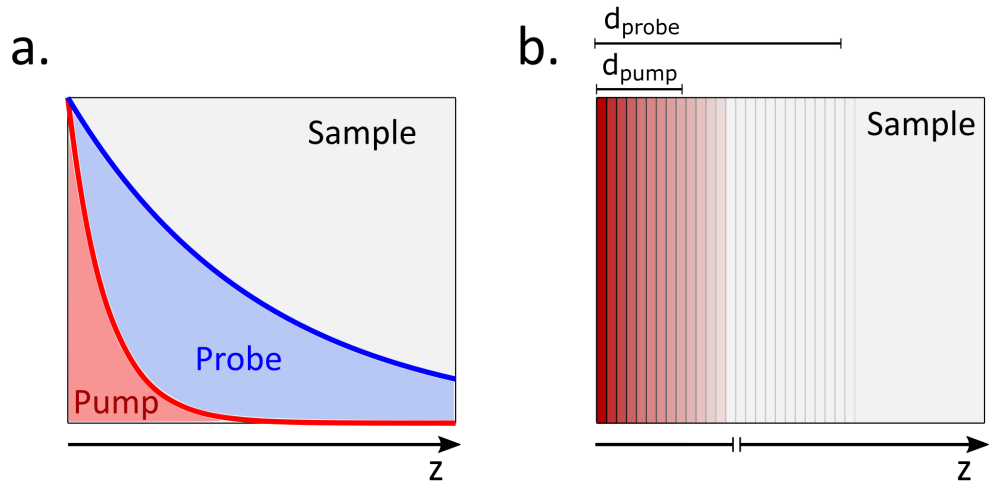

Figure 5.7: Multi-layer model representation. It takes into account that the fields are absorbed exponentially in a material.

the pump pulse only creates the uniformly photo-excited region of thickness d_{pump}.

From the measured electro-optic traces, one extracts $r'(\tilde{\omega}, \tau)$; from $r'(\tilde{\omega}, \tau)$, by means of the system 5.3, the complex refraction index N_1' of the photo-excited material, for a given pump-probe time delay τ. This last quantity is what we are interested in, since it allows us to extract all the optical constants of the photo-excited material, as has been shown in equations 5.2.

The assumption that the material is uniformly photo-excited is reasonable, but we know that this is not the reality, since beams are not uniformly absorbed by each layer of the photo-excited part of the sample. To take into account the exponential absorption of the fields, the *multi-layer* model has been used to extract the optical quantities of the photo-excited material.

5.2 Experimental results

Here we show the results from our experiment. Time-resolved THz spectroscopy was performed to separately drive the two vibrational modes in $YBa_2Cu_3O_{6.5}$ associated with the displacement of the apical oxygen in the Cu-O oxygen-rich and oxygen-deficient chains - respectively at 16.46 THz and 19.28 THz - , and to follow the transient dynamics of the sample. To be more confident about the conclusions we drew, we decided to pump the system even out of resonance, at 21.58 THz. In Figure 5.8, we show the optical properties along the c-axis of the material, acquired 0.9 ps after excitation of the phonon-mode at 19.28 THz above T_c (T_c=53 K), at 100K . We focus here on this mode because it is the one with the clearest signatures of enhancement of superconductive coupling between bilayers. We plot differential quantities like $\Delta\sigma_2(\bar{T}) = \sigma_2^{excited}(\bar{T}) - \sigma_2^{equilibrium}(\bar{T})$, in order to remove the background due to normal transport at equilibrium [33]. We find all the signatures of superconducting transport along the c-axis that we expect from the discussion in Section 4.2. We can see from the data that $\Delta\sigma_2$ really increases when $\omega \rightarrow 0$. We recall that the Drude-Lorentz model of charge conduction predicts that, in case of zero dissipation, $\sigma_2 \propto \frac{1}{\omega}$. Then, $\Delta\sigma_1$, in Figure (b), shows an enhancement of coherent transport going toward zero frequency. In Figure (c) it is present the low frequency edge in the relative reflectivity that is a clear signature of coherent tunnelling between bilayers. Exactly the same conclusion can be drawn from the appearance of the peak in the differential loss function at the same frequency, $\omega_{J_{p1}}$. Notice that from the discussion in Section 4.2 we learned that the Josephson coupling energy term between superconducting layers,J, is proportional to $\frac{\omega_{J_{p1}}^2 \omega_{J_{p2}}^2}{\omega_T^2}$. Since in our sample, in the superconductive state, $\omega_{J_{p2}} \approx \omega_T \gg \omega_{J_{p1}}$, this implies that $J \propto \omega_{J_{p1}}^2$. Now, we saw from Figure (c) and (d), that $\omega_{J_{p1}}$ above T_c in

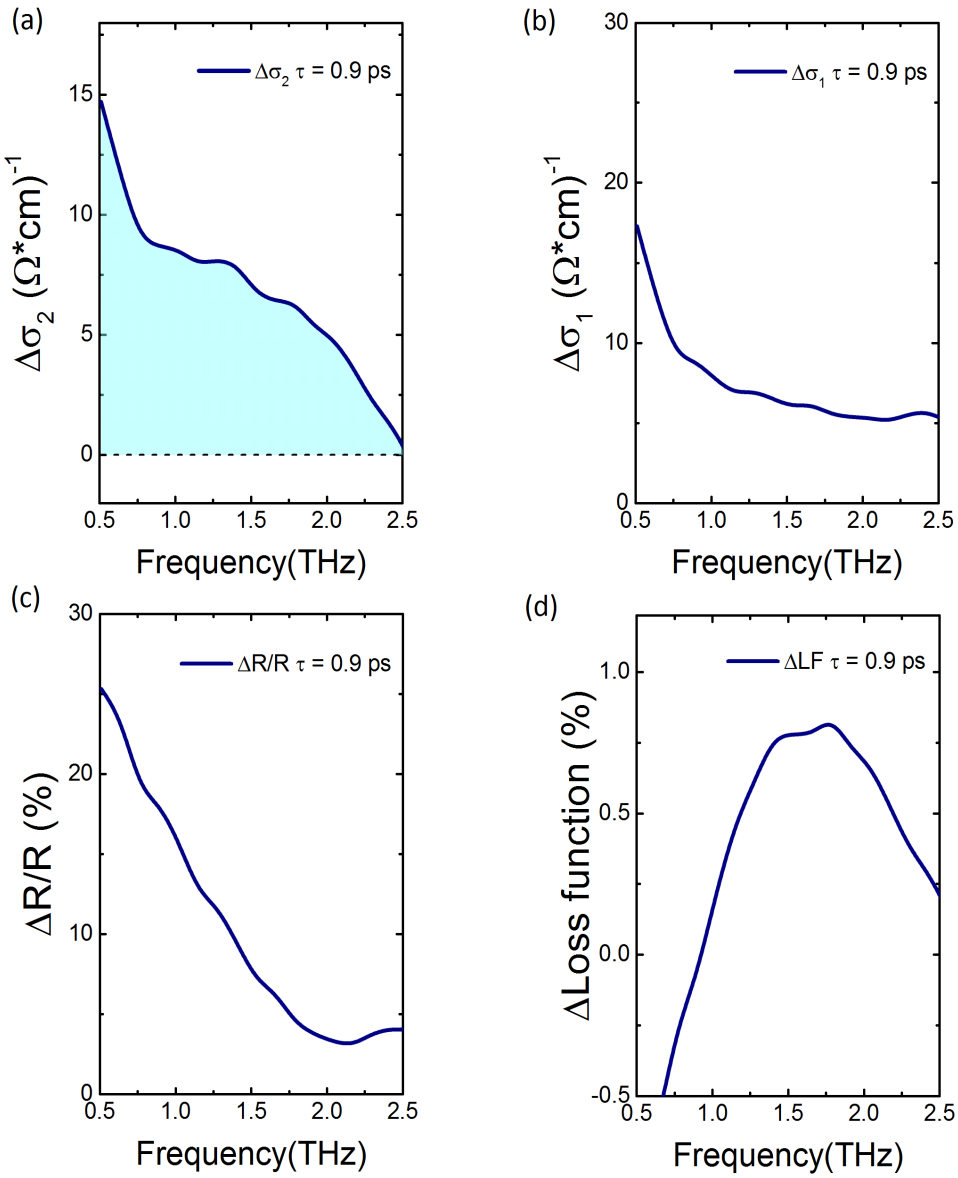

Figure 5.8: Optical properties of $YBa_2Cu_3O_{6.5}$ 0.9 ps after the excitation with 19.28 THz pump, take at 100 K temperature (above T_c). (a): enhancement of $\Delta\sigma_2(\omega)$ as $\omega \rightarrow 0$. (b): $\Delta\sigma_1$ shows an enhancement of coherent transport going toward zero frequency. (c): appearance of the low-frequency edge in relative reflectivity. (d): appearance of a peak in the loss function at the same frequency of the edge in reflectivity.

the transient state is around 2 THz, while we know from Figure 4.6 that at equilibrium below T_c it is around 1 THz. This suggests that the coherent coupling between bilayers induced in the transient state by resonantly pumping the 19.28 THz phonon is almost four times higher than in the equilibrium superconducting state.

The next step was to extract the vale of $\omega\Delta\sigma_2|_{\omega\to 0}$ for each pump frequency and each time delay, for the maximum achievable value of the electric field ($\approx$ 3.3 MV/cm). This value is proportional, in fact, to the Josephson coupling J, and to the superconductive density along the c-axis (see Formula 4.1). Figure 5.9 shows the promp appearance of finite superconducting density, revealing the formation dynamics of a 3D superconducting-like state. The peak value of $\omega\Delta\sigma_2|_{\omega\to 0}$ is almost two times higher for the phonon at 19.28 THz with respect to the one at 16.46 THz. Both of them are higher than the value of the out-of-resonance excitation. The lifetime of the light-induced state can be fit in all the cases with a double exponential function. The shortest decay time is $\approx$ 0.55 ps in the higher-frequency mode while in the case of the low-frequency mode and out-of-resonance pumping it is respectively 0.3 ps and 0.2 ps. It is worth recalling that the time duration of the pump-pulse was $\approx$ 0.55 ps. The longest decay time is $\approx$ 5 ps for all the three curves.

At this point we decided to perform a pump-electric field-dependent measurement. The characteristic of the pump were the same than in the previous measurements, the only difference its that the electric field was linearly attenuated by means of two wire-grid polarisers. The data are shown in Figure 5.10. As we expected from our previous measurements, the slope of the curves that represent $\omega\Delta\sigma_2|_{\omega\to 0}$ as a function of the amplitude of the pump electric field is higher for the phonon at 19.28 THz, decreases for

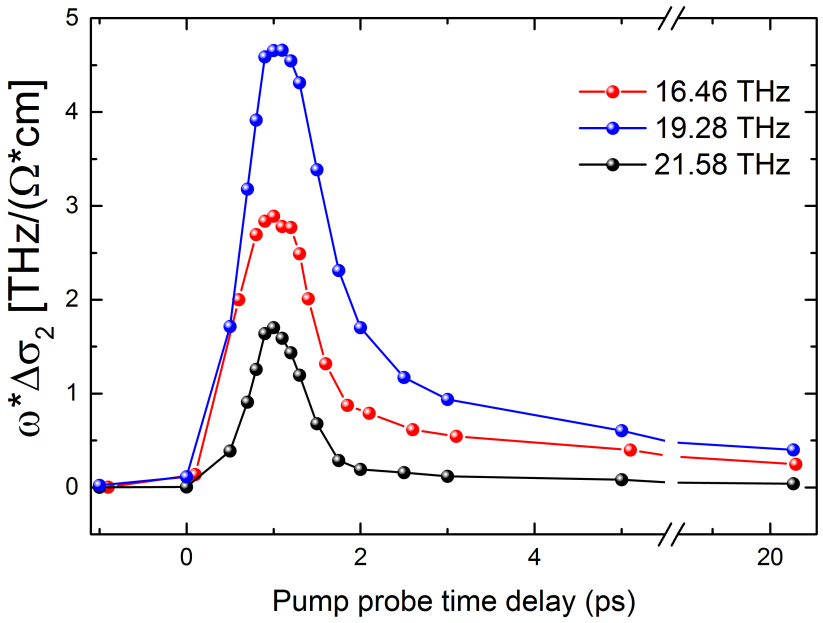

Figure 5.9: Superfluid-density in the c-axis as a function of the pump-probe time delay τ. Measured taken above T_c at 100 K; the peak electric field was 3.3 MV/cm for all the data points; duration of the pump-pulse 0.55 ps. The peak value of $\omega\Delta\sigma_2|_{\omega\to 0}$ is almost two times higher for the phonon at 19.28 THz with respect to the one at 16.46 THz. Both of them are higher than the value of the out-of-resonance excitation. The lifetime of the light-induced state can be fit in all the cases with a double exponential function. The shortest decay time is $\approx$ 0.55 ps in the higher-frequency mode while in the case of the low-frequency mode and out-of-resonance pumping it is respectively 0.3 ps and 0.2 ps.

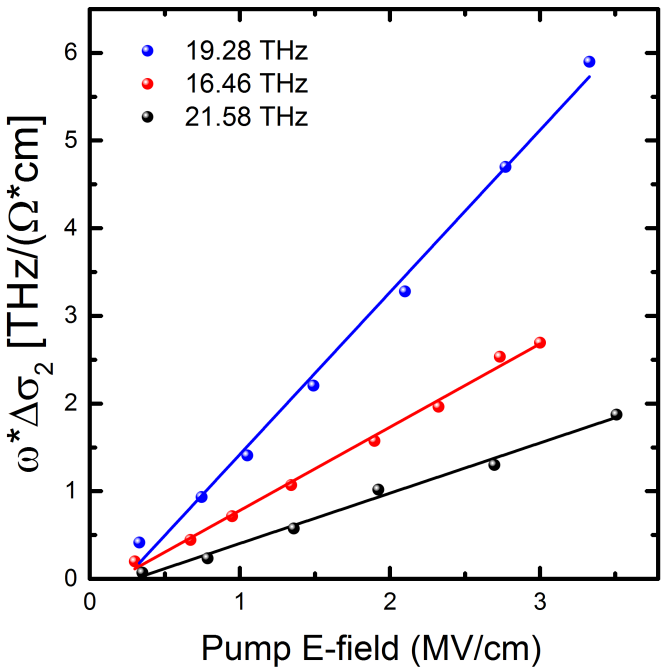

Figure 5.10: Amplitude of the pump's electric field-dependence of the superconducting density along the c-axis for the three pump-frequencies above mentioned. The response is linear for all of them.

the phonon at 16.46 THz, and assumes the lowest value in case of out-of-resonance pumping. More interestingly, all the curves show that the superconducting density along the c- axis, or the Josephson coupling in the interbilayer region, scales linearly with the amplitude of the peak value of the pumping electric field $|E_{pump}|$. It is worth at this point recalling some concepts from nonlinear phononic theory. For pulses that are short compared with the many-picoseconds decay time of optical phonons [49], one can ignore dissipation and the first equation of the system of equations 4.4 becomes: $\ddot{Q}_{IR} + \omega_{IR}^2 Q_{IR} = f(t)$, where $f(t) = E_0 F(t) \sin(\omega_{IR} t)$ (see Section 4.4). At times much longer than the pulse width:

$$Q_{IR}(t) \propto \tau_{pump} E_0 \tag{5.4}$$

The equation of motion for the Raman-active mode(s) with which the IR-active mode nonlinearly couples is, from the second equation of system 4.4, considering null the dissipation: $\ddot{Q}_R + \omega_R^2 Q_R = a_{21} Q_{IR}^2$. For $\omega_{IR} \gg \omega_R$ - that holds in our case, since we know from [37] that the Raman modes with which the investigated IR-active modes at 16.46 and 19.28 THz couple oscillate at approximately 3 THz - we have:

$$Q_R(t) \propto \tau_{pump}^2 E_0^2 \tag{5.5}$$

Combining these results with the one shown in Figure 5.10 we can conclude that, according to the theory of nonlinear phononics, the Josephson coupling J in the interbilayer region - or the superconducting density along the c-axis - is proportional to the amplitude of the IR-active driven mode and to the square root of the dispalcement of the Raman mode(s) to which to IR-mode couples:

$$\rho_c \propto Q_{IR} \propto \sqrt{Q_R} \tag{5.6}$$

Finally we want to show one last result. We extracted from Figure 5.10 the slope of $\omega\Delta\sigma_2|_{\omega\to 0}$ for the three curves and we plot the three values obtained in the same graph, together with the optical conductivity $\sigma_1(\omega)$ at 100K. We choose the slope of $\omega\Delta\sigma_2|_{\omega\to 0}$ as susceptibility rather than simply $\omega\Delta\sigma_2|_{\omega\to 0}$ because it takes into account all the measurements performed for different values of the maximum amplitude of the pump electric field. The value of σ_1 for a given ω - we know from electrodynamics of continuous media [50]- is proportional to the amount of electromagnetic energy absorbed by the medium when a wave at frequency ω propagates through it. $\sigma_1(\omega)$ peaks in correspondence of the phonon modes. We see from the red curve in Figure 5.11 that the phonon at 19.28 has a bigger spectral weight than the one at 16.46 THz. So, it absorbs more energy from the electromagnetic field. In correspondence of that phonon we see the highest superconducting response. One might hypothesize that the phonon at 19.28 THz, that gained more energy from the driving field, can transfer more energy to the lattice dynamics - through nonlinear coupling with Raman-active modes - creating in this way a displacive lattice structure that favours superconducting tunnelling above T_c in the interbilayer region.

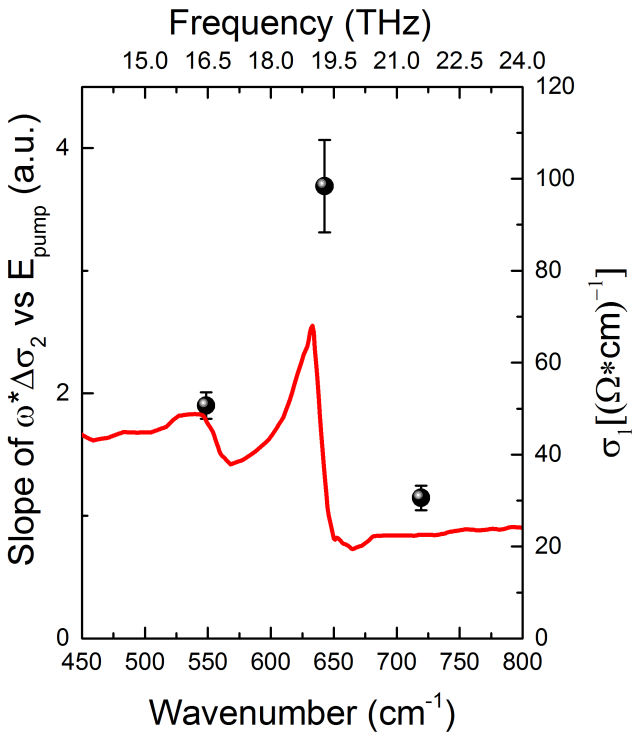

Figure 5.11: Plot of the value of the slope of $\omega\Delta\sigma_2$ (data points), as extracted from the field dependent measurements, and of the real part of the c-axis conductivity (red lines, from literature), both as a function of the frequency of the exciting pump pulse.

Chapter 6

Conclusions & Outlook

The goal of the present thesis was to setup a mid-infrared pulsed light source sufficiently narrowband and tunable to drive separately the two near-degenerate apical oxygen phonon modes in the bilayer cuprate YBCO. Earlier works have shown that, by driving both modes simultaneously, a transient short-lived superconducting state can be induced above the equilibrium critical temperature. Exploiting the contributions of the individual modes, potentially could pave the way for a better understanding of the light-induce superconductivity in underdoped cuprates.

In the course of the thesis project, we managed to use chirped pulse difference frequency generation in a GaSe nonlinear crystal to produce narrowband mid-infrared carrier-envelope phase stable pulses with a minimum relative bandwidth $\frac{\Delta E}{E}$ of 2 % , tunable between 16 THz and 23 THz. The duration of these pulses scaled with the bandwidth, which can be chosen by the amount of chirp imprinted on the generating near-infrared pulses between 200 fs and 1 ps. The energy of the mid-infrared pulses around 8 μJ could be kept constant even for the different pulse durations by adjusting the spot sizes in the GaSe nonlinear crystal to maintain the gain coefficient.

This source was then used, possibly for the first time, to clearly distinguish the effect of driving the individual vibrational modes, on the light-induced superconducting state. The response of the material was monitored -with pump-probe time-resolved THz spectroscopy- on a subpicosecond time scale by measuring the reflection changes of a delayed 'probe' pulse at THz frequencies, induced by the pump pulse. In that frequency regime indeed can be found the fingerprints of the superconducting light-induced state.

The data showed, firstly, that the strength of the light-induced superconducting state linearly increases with the amplitude of the driving electric field. According to the theory of nonlinear phononics, this implies that ρ_c scales with the square root of Q_R, where Q_R is the amplitude of the displacement of the crystal structure along the Raman-active mode coordinates. This displacements corresponds to the reduction in the distance between CuO_2 bilayers. Secondly, the strength of the transient superconducting coupling between bilayers above the equilibrium critical temperature – measured through the value of transient superfluid density along the c-axis, ρ_c – was found to be much higher for the phonon at 19.28 THz that, between the two investigated, has the biggest spectral weight.

These two conclusions, respectively, suggest that in the future would be interesting to: quantify by means of time-resolved x-ray measurements the variation of the inter- and intra-bilayers distance due to each one of the two individually driven apical oxygen vibrations, to experimentally verify if $\rho_c \propto \sqrt{Q_R}$; secondly, drive some low-lying THz-frequency phonon modes that have a spectral weight much higher than the ones investigated [35], to see whether the effect on the strength of the superconducting-induced state is bigger, as one expected from the second conclusion. In this regard, we remark that our novel pump-scheme may also be extended to frequencies

lower than the ones used here, enabling selective excitation in the *THz gap* between 4 and 15 THz [25]. Finally, one could exploit the time-duration tunability of our pump-pulses to investigate how the duration of the transient superconducting state scales with the pump pulse duration.

All this can be useful to draw even more general conclusions on the microscopic mechanism that drives the light-induced superconducting state and on the feasibility of a real-life application of this fascinating phenomenon.

Acknowledgements

I would like to thank Prof. Andrea Cavalleri for having given me the opportunity to join his Group at the Max Planck Institute of Hamburg.

My gratitude also goes to my supervisor from Politecnico di Milano, Prof. Giulio Cerullo. Thank you for your precious advice and for your endless willingness. I would like to acknowledge Prof. Arianna Montorsi for being my supervisor from Politecnico di Torino.

Special word of thanks must go to Dr. Michael Foerst . I am grateful for your exhaustive explanations and for your precious suggestions. In writing my thesis, I was inspired by your capability of extracting the central information from a complex physical problem and conveying it in the clearest way. My acknowledgment also goes to Biaolong. Thank you for all you taught me in the lab, for your help, and for your patience in answering all my questions. I also want to thank my colleagues at the MPSD. Thanks in random order to Tobia, Alice, Daniele, Michele, Ankit, Gregor, Srivats, Ken, Andrea Cartella, Eryin, Matthias, Dawei, Alex, Benedikt, Thomas, and Daniel. It has been a unique privilege to learn from discussions with you.

I ringraziamenti piu‘ sentiti vanno ai miei genitori. L‘amore che provate per noi vi ha consentito di lasciarci andare quando avevamo appena diciotto anni. E di non chiederci mai di tornare, anche adesso che gli studi sono conclusi. Posso solo dire che mi rendo conto del sacrificio che questo richiede,

che mancate tanto anche voi a me e che vi voglio bene.

Grazie a mio fratello, che sembra un insensibile ma quando ho bisogno c'e' sempre.

Grazie a tutti gli altri familiari, anche quelli che non ci sono piu', e agli amici di sempre.

Grazie, infine, a Sara. Averti incontata e' stata la fortuna piu' grande che mi sia capitata.

Bibliography

[1] C. Manzoni and G. Cerullo, *J.Opt*, **18**, 103501 (2016).

[2] Robert Boyd, Nonlinear Optics, *Academic Press* (2003).

[3] A. Schneider, M. Neis, M. Stillhart, B. Ruiz, R. Khan, and P. Günter, *JOSA B* **23**, 9 (2006).

[4] G. Cerullo and S. De Silvestri, *Review of Scientific Instruments*, **74**, 1 (2003).

[5] Ka-Lo Yeh, Janos Hebling, Matthias C. Hoffmann, Keith A. Nelson, *Optics Communications*, **281**, 3567-3570 (2008).

[6] Ka-Lo Yeh, M. C. Hoffmann, J. Hebling, and Keith A. Nelson, *Appl. Phys. Lett.* **90**, 171121 (2007).

[7] R. Huber, A. Brodschelm, F. Tauser, and A. Leitenstorfer, *Appl. Phys. Lett.*, **76**, 3191 (2000).

[8] D. R. Suhre, N. B. Singh, V. Balakrishna, N. C. Fernelius, and F. K. Hopkins, *Opt. Lett.* **22**, 775-777 (1997).

[9] H. Hirori, F. Blanchard, and K. Tanaka, *Appl. Phys. Lett.*, **98**, 9 (2011).

[10] F. Blanchard, L. Razzari, H.C. Bandulet, G. Sharma, R. Morandotti, J.C. Kieffer, T. Ozaki, M. Reid, H. F. Tiedje, H. K. Haugen, and F. A. Hegmann6, *Optics Express*, **15**, 20 (2007).

[11] Matthias C. Hoffmann, Ka Lo Yeh, Janos Hebling and Keith A. Nelson, *Optical Society of America*, **18**, 15 (2007).

[12] D. Redfield and W. J. Burke, *J. Appl. Phys.* **45**, 4566-4571 (1974).

[13] Marcel Stillhart, Arno Schneider, and Peter Günter,*J. Opt. Soc. Am. B* **25**, 1914-1919 (2008).

[14] Christoph P. Hauri, Clemens Ruchert, Carlo Vicario, and Fernando Ardana *Appl. Phys. Lett.* **99**, 161116 (2011).

[15] M. Shalaby and C.P. Hauri, *Nature Communications* **6**, 5976 (2015).

[16] D.A. Roberts, *IEEE JQE* **28** 2057 (1992).

[17] U. Meier, M. Bösch, Ch. Bosshard, F. Pan, and P. Günter, *Journal of Applied Physics***83**, 3486 (1998).

[18] Lukas Mutter, Fabian D. J. Brunner, Zhou Yang, Mojca Jazbinšek, and Peter Günter, *J. Opt. Soc. Am.B* Vol. 24, No. 9 (2007)

[19] Alexander Sell, Alfred Leitenstorfer, and Rupert Huber, *Optics Letters* Vol. 33, Issue 23, pp. 2767-2769 (2008).

[20] K. Reimann, R. P. Smith, A. M. Weiner, T. Elsaesser, and M. Woerner, Optics Letters Vol. 28, Issue 6, pp. 471-473 (2003).

[21] Matthias C Hoffmann, József András Fülöp, *Journal of Physics D: Applied Physics*, 2011, **44** (8), pp.83001.

[22] Cristian Manzoni, Michael Först, Henri Ehrke, and Andrea Cavalleri, *Optics Letters* Vol. 35,**5**, pp. 757-759 (2010).

[23] A. Baltuška, T. Fuji, and T. Kobayashi, *Phys. Rev. Lett.*, **88**, 133901 (2002).

[24] R. L. Aggarwal and B. Lax, in *Nonlinear Infrared Generation* (Springer, New York, 1977), p. 28.

[25] B. Liu, H. Bromberger, A. Cartella, T. Gebert, M. Först, and A. Cavalleri, *Optics Letters* Vol. 42, **1**, pp. 129-131 (2017)

[26] A. Cartella, T. F. Nova, A. Oriana, G. Cerullo, M. Först, C. Manzoni, and A. Cavalleri, *Optics Letters* 42' **4**, (2017)

[27] Backus S, Durfee C G, Murnane M M, Margaret M and Kapteyn H C, *Rev. Sci. Instrum.* 69 1207–23 (1998)

[28] Rini, M., Tobey, R., Dean, N., Itatani, J., Tomioka, Y., Tokura, Y., Schoenlein, R. W., and Cavalleri, A. Control of the electronic phase of a manganite by mode-selective vibrational excitation. Nature 449(7158), 72–74 (2007)

[29] Caviglia, A. D., Scherwitzl, R., Popovich, P., Hu, W., Bromberger, H., Singla, R., Mitrano, M., Hoffmann, M. C., Kaiser, S., Zubko, P., Gariglio, S., Triscone, J. M., Först, M., and Cavalleri, A. Ultrafast strain engineering in complex oxide heterostructures. Physical Review Letters 108(13), 136801 (2012).

[30] Först, M., Tobey, R. I., Wall, S., Bromberger, H., Khanna, V., Cavalieri, A. L., Chuang, Y. D., Lee, W. S., Moore, R., Schlotter, W. F., Turner, J. J., Krupin, O., Trigo, M., Zheng, H., Mitchell, J. F., Dhesi, S. S.,

Hill, J. P., and Cavalleri, A. Driving magnetic order in a manganite by ultrafast lattice excitation. Physical Review B - Condensed Matter and Materials Physics 84(24), 241104 (2011).

[31] Först, M., Caviglia, A. D., Scherwitzl, R., Mankowsky, R., Zubko, P., Khanna, V., Bromberger, H., Wilkins, S. B., Chuang, Y.-D., Lee, W. S., Schlotter, W. F., Turner, J. J., Dakovski, G. L., Minitti, M. P., Robinson, J., Clark, S. R., Jaksch, D., Triscone, J.-M., Hill, J. P., Dhesi, S. S., and Cavalleri, A. Spatially resolved ultrafast magnetic dynamics initiated at a complex oxide heterointerface. Nature Materials 14(9), 883–888 (2015).

[32] Fausti, D., Tobey, R. I., Dean, N., Kaiser, S., Dienst, A., Hoffmann, M. C., Pyon, S., Takayama, T., Takagi, H., and Cavalleri, A. Light-induced superconductivity in a stripe-ordered cuprate. Science 331(6014), 189–191 (2011).

[33] Kaiser, S., Hunt, C. R., Nicoletti, D., Hu, W., Gierz, I., Liu, H. Y., Le Tacon, M., Loew, T., Haug, D., Keimer, B., and Cavalleri, A. Optically induced coherent transport far above Tc in underdoped YBa2Cu3O6+x. Physical Review B 89(18), 184516 (2014).

[34] Hu, W., Kaiser, S., Nicoletti, D., Hunt, C. R., Gierz, I., Hoffmann, M. C., Le Tacon, M., Loew, T., Keimer, B., and Cavalleri, A. Optically enhanced coherent transport in YBa2Cu3O6.5 by ultrafast redistribution of interlayer coupling. Nature materials 13(May), 705–711 (2014).

[35] C.C.Homes et al., Can.J.Phys.73:663-675(1995)

[36] Roman Mankowsky et al 2016 Rep. Prog. Phys. 79 064503

[37] Roman Mankowsky et al, 4 DECEMBER 2014 — VOL 516 — NATURE — 71

[38] C.C. Homes, T. Timusk, and D.A. Bonn, R. Liang and W.N. Hardy, Can. J. Phys. 73: 663–675 (1995)

[39] D.van der Marel, Journal of Superconductivity, Vol.17, No.5, October 2004

[40] M.Thinkhan, Introduction to Superconductivity: Second Edition, Dover Books on Physics, 2004

[41] D.van der Marel and A.Tsvetkov, Czechoslovak Journal of Physics, Vol.46 (1996)

[42] Huber, J. G. and Liverman, W. J., Physical Review B 41(13), 8757–8761 (1990).

[43] Schirber, J. E., Ginley, D. S., Venturini, E. L., and Morosin, B. Physical Review B 35(16), 8709–8710 (1987).

[44] Bucher, B., Karpinski, J., Kaldins, E., and Wachter, P. Journal of Less-Common Metals 164, 165, 20–30 (1990).

[45] G.Ghiringhelli et al., Science 337(6069), 821-825(2012)

[46] M.Foerst et al., Physical Review Letters 112(15), 157002 (2014)

[47] D. Fausti et al., Science 331(6014), 189-191(2011)

[48] M.Foerst et al., Nature Physics, 7, pages 854–856 (2011)

[49] Von der Linde, D. and Lambrich, R., Phys. Rev. Lett. 42, 1090–1093 (1979)

[50] John David Jackson Classical Electrodynamics John Wiley and Sons Ltd. 1962